



The middle-to-late Eocene greenhouse climate, modelled using the CESM 1.0.5

Michiel Baatsen¹, Anna S. von der Heydt¹, Matthew Huber², Michael A. Kliphuis¹, Peter K. Bijl³, Appy Sluijs³, and Henk A. Dijkstra¹

¹Institute for Marine and Atmospheric Research, Department of Physics, Utrecht University, Princetonplein 5, 3584CC Utrecht, Netherlands

²Purdue University, 610 Purdue Mall, West Lafayette, IN, 47906 USA

³Department of Earth Sciences, Marine Palynology and Paleoceanography, Laboratory of Palaeobotany and Palynology, Utrecht University, Princetonlaan 8a, 3584 CB Utrecht, the Netherlands

Correspondence to: Michiel Baatsen (m.l.j.baatsen@uu.nl)

Abstract. While the early Eocene has been considered in many modelling studies, detailed simulations of the middle and late Eocene climate are currently scarce. To get a better understanding of both Antarctic glaciation at the Eocene-Oligocene transition (~34Ma) and late middle Eocene warmth, it is vital to have an adequate reconstruction of the middle-to-late Eocene climate. Results of higher (CMIP5-like) resolution coupled climate simulations are represented here using the Community Earth System Model (CESM) version 1. Two middle-to-late Eocene cases are considered with the same general boundary conditions but a different radiative forcing, using a new detailed 38Ma geography reconstruction.

Under $4\times$ pre-industrial concentrations (PIC) of both CO_2 (i.e. 1120ppm) and CH_4 (~2700ppb), equilibrium sea surface temperatures correspond well to the available late middle Eocene (42–38 Ma; ~Bartonian) proxies. Being generally cooler, the simulated climate under $2\times$ PIC forcing is a good analog for that of the late Eocene (38–34 Ma; ~Priabonian). Terrestrial temperature proxies, although their geographical coverage is sparse, also indicate that the results presented here are realistic.

The reconstructed 38Ma climate has a reduced equator-to-pole temperature gradient and a more symmetric meridional heat distribution compared to the pre-industrial reference. The collective effects of geography, vegetation and ice accounts for a global mean $5\text{--}7^\circ\text{C}$ difference between pre-industrial and 38Ma Eocene boundary conditions, with important contributions from cloud and water vapour feedbacks. These simulations effectively show that a realistic middle-to-late Eocene climate can be reconstructed without the need for greenhouse gas concentrations much higher than proxy estimates (i.e. ~500–1200 ppm CO_2).



Equilibrium climate sensitivity is reduced ($0.62\text{ }^{\circ}\text{C}/\text{Wm}^2$; 3.2°C warming between 38Ma $2\times$ PIC and $4\times$ PIC) compared to that of the present-day climate ($0.79\text{ }^{\circ}\text{C}/\text{Wm}^2$; 3.1°C per CO_2 doubling). Despite very limited sea ice and snow cover in both 38Ma cases, the model still shows a factor ~ 2 polar amplification in response to a further increase of atmospheric greenhouse gas concentrations. High latitudes in the modelled Eocene climate are mainly kept warm by an altered radiative balance in combination with global changes in geography and the absence of polar ice sheets compared to the pre-industrial reference.



30 1 Introduction

The Eocene-Oligocene transition (EOT) is one of the most dramatic climate transitions of the Cenozoic, thought to be associated with the formation of a continental-scale ice sheet on Antarctica (Zachos et al., 1994; Coxall et al., 2005; Lear et al., 2008). A possible cause for the inception of ice is a long-term decline of greenhouse gas concentrations through the middle Eocene, eventually crossing a threshold for glaciation (DeConto and Pollard, 2003; DeConto et al., 2008; Gasson et al., 2014). Following the early Eocene (~50Ma), a gradual cooling levelled off during the middle Eocene (43–42 Ma) and eventually reversed into a warming (Zachos et al., 2001, 2008; Bijl et al., 2009; Cramwinckel et al., 2018) towards the Middle Eocene Climatic Optimum at ~40Ma (MECO; Bohaty and Zachos 2003; Bijl et al. 2010; Sluijs et al. 2013). The cooling trend continued during the late Eocene (~38–34 Ma), with a cold interval at ~37.3Ma characterised by the Priabonian Oxygen isotope Maximum (PrOM, Scher et al. 2014). While these temperature changes may have caused some ice growth as early as the middle Eocene, they did not allow the formation of a continental-scale Antarctic ice sheet until after 34Ma (Scher et al., 2014; Passchier et al., 2017; Carter et al., 2017). It remains a question to what extent continental geometry (e.g. opening of Southern Ocean Gateways) next to gradual shifts in both the atmospheric and oceanic circulation, was a driver to both regional and global climate change during the Eocene (Bijl et al., 2013; Bosboom et al., 2014; Sijp et al., 2014, 2016).

The climate throughout most of the Eocene was characterised by a reduced equator-to-pole temperature gradient compared to what is seen today (Bijl et al., 2009; Hollis et al., 2012; Douglas et al., 2014; Evans et al., 2018). This aspect of the Eocene greenhouse climate has proven challenging to simulate adequately with climate models (Huber and Sloan, 2001; Huber and Caballero, 2011; Cramwinckel et al., 2018). Very high greenhouse gas concentrations were often needed to reproduce high-latitude warmth at the expense of equatorial temperatures being significantly higher than indicated by proxy data (Huber and Caballero, 2011; Lunt et al., 2012). Estimates of the meridional temperature gradient during the Eocene have come up with respect to some earlier studies, mainly due to higher equatorial temperatures (Pearson et al., 2007; Schouten et al., 2013; Inglis et al., 2015; Evans et al., 2018; Cramwinckel et al., 2018). Meanwhile, numerical climate models have been under continuous development by including more processes (especially cloud properties, e.g. Abbot et al. 2009; Kiehl and Shields 2013) and using a higher spatial resolution with better resolved palaeogeographies (Baatsen et al., 2016; Lunt et al., 2016; Hutchinson et al., 2018) to improve the overall model-proxy consensus.

While many modelling studies have focussed on the early Eocene (Huber and Caballero, 2011; Lunt et al., 2012; Herold et al., 2014; Zhu et al., 2019), others have looked at the latest Eocene - early Oligocene (Hill et al. 2013; Ladant et al. 2014; Kennedy et al. 2015 see also the overview of Gasson et al. 2014), with little attention to most of the middle Eocene. Licht et al. (2014) performed simu-



lations with both a 40Ma and 34Ma geography reconstruction, using a reduced complexity climate model (FOAM). A comprehensive model study with several time slices covering the Eocene is presented by Inglis et al. (2015); Lunt et al. (2016); Farnsworth et al. (2019) using a lower resolution
70 version of the HadCM3 model. Cramwinckel et al. (2018) provide an overview of different climatic states throughout the middle Eocene cooling using the CCSM3 simulations of Goldner et al. (2014).

Here, we present the results of a set of coupled atmosphere-ocean simulations with the Community Earth System Model (CESM) version 1.0.5 using the 38Ma boundary conditions of Baatsen
75 et al. (2016). With time-specific geographic boundary conditions, a CMIP-5 like model and adequate equilibration, the aim is to show a more detailed and representative model-based overview of the middle-to-late Eocene (i.e. Bartonian–Priabonian; ~42–34 Ma) climate. The considered period is suitable to investigate both the warm greenhouse climate as the conditions leading up to the EOT. The focus will therefore be on the general features of the modelled climate, a comparison
80 to proxies as well as other model results, and the similarities/differences with the present climate (specifically regarding climate sensitivity).

The model set-up and spin-up procedure for the CESM simulations are first explained in section 2. The main results are then presented in section 3 including the equilibrium climate of each simulation (3.1), a model-proxy comparison (3.2) and a model-model comparison (3.3). This is followed
85 by an analysis of equilibrium climate sensitivity derived from the different simulations in section 3.4, with a focus on the main changes involved in the radiative balance. Finally, our main findings are summarised and discussed in section 4.



2 Methods

2.1 The CESM 1.0.5

90 The Community Earth System Model (CESM; Hurrell et al. 2013) version 1 is a fully coupled
atmosphere-land-ice-ocean general circulation model (GCM) that was developed at the National
Center for Atmospheric Research (NCAR) in Boulder, Colorado. For use in palaeoclimate mod-
elling, version 1.0.5 of the CESM is a suitable choice motivated by a trade-off between increasing
model complexity and computational cost. The model as used here is equivalent to the latest version

95 4 of the CCSM (Blackmon et al., 2001; Gent et al., 2011).

The atmospheric component of the CESM is the Community Atmosphere Model (CAM4; Neale
et al. 2013) and uses a finite volume grid at a nominal resolution of 2° ($2.5^\circ \times 1.9^\circ$) and 26 vertical
levels with a hybrid sigma vertical coordinate extending upward to 2hPa. In this configuration, the
model has a reported warming response of 3.13°C to a doubling of CO_2 starting from pre-industrial
100 conditions (Bitz et al. 2012, compared to $\sim 2.5^\circ\text{C}$ in CCSM3; Kiehl et al. 2006).

The physical, chemical and biological processes taking place on land are represented in the Com-
munity Land Model (CLM4; Oleson et al. 2010; Lawrence et al. 2011), in which all anthropogenic
influences are disregarded. A static rather than dynamic vegetation model is used here to avoid run-
away feedback effects, which can become an issue especially in warm greenhouse climates (e.g.
105 dieback of vegetation at low latitudes; Loftson et al. 2014; Herold et al. 2014). The considered
biomes are translated into fractions of the corresponding CLM4 plant functional types (PFTs), from
which a set of monthly forcing files is finally used in the model.

The sea ice component consists of the Los Alamos National Laboratory (LANL) Community Ice
Code version 4 (CICE4; Hunke and Lipscomb 2008). For simplicity, sea ice only forms when the
110 sea surface cools down to -1.8°C , after which its dynamical behaviour is treated by the model specif-
ically.

The CESM1 uses the LANL Parallel Ocean Program version 2 (POP2; Smith et al. 2010) for the
ocean model component. The standard configuration is applied here, with a nominal 1° ($1.25^\circ \times 0.9^\circ$)
horizontal resolution on a curvilinear grid placing the northern pole over Greenland. In the vertical,
115 the POP2 is set up with 60 layers of varying thickness between 10m near the surface and 250m
at greater depth. Horizontal viscosity is considered anisotropic (Smith and McWilliams, 2003) and
horizontal tracer diffusion follows the parameterisation of Gent and McWilliams (1990). The model
further uses the KPP-scheme to determine vertical mixing coefficients (Large et al., 1994). More
information and discussion on the ocean model physics and parameterisations can be found in Dan-
120 abasoglu et al. (2008, 2012).



2.2 Model Experiments

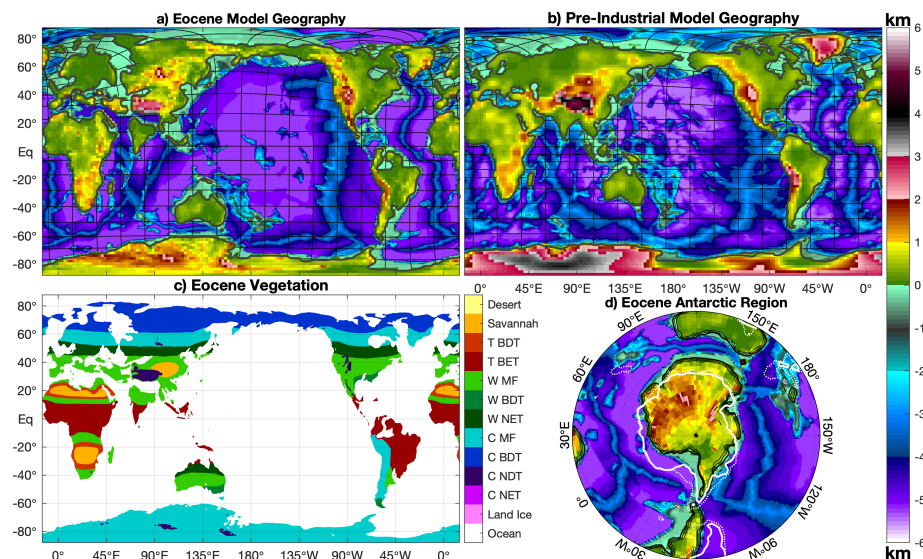


Figure 1. Topography (atmosphere) and bathymetry (ocean) grid used in the model simulations for the **a)** 38Ma Eocene cases and **b)** pre-industrial reference. Black lines are drawn every 20 model grid boxes for the ocean and the thick grey line shows the coastlines at 0.5 land fraction. **c)** Vegetation biomes for the Eocene cases (with **T:** tropical–**W:** warm–**C:** cool, and **B:** broadleaf–**N:** needleleaf; **D:** deciduous–**E:** evergreen; **MF:** mixed forest–**T:** tree), note that neither desert nor land ice are implemented. **d)** South polar stereographic projection of the 38Ma model geography, with white contours indicating pre-industrial coastline (solid) and 1km depth (dashed).

To allow comparisons of various climatic features between Eocene and pre-industrial conditions within a similar framework, a pre-industrial reference run with the same version of the CESM is performed (using the geography shown in Figure 1b). Since the atmospheric component used here
125 consists of the CAM4 at a nominal 2° horizontal resolution (Figure 1a), this reference is similar to the 2° 1850 control from Gent et al. (2011). The solar constant in the simulation is 1361W/m^2 and the atmospheric levels of CO_2 and CH_4 are 280ppm and 671ppb, respectively (i.e. pre-industrial carbon; PIC). Astronomical orbital parameters are set to their present-day configurations; eccentricity: 0.0167, obliquity: 23.44° and precession placing the aphelion in Northern Hemisphere summer. Both
130 vegetation and atmospheric aerosols are kept fixed at their respective pre-industrial distributions.

For deep-time climate simulations there are a number of model parameters and settings that need to be reconsidered, while others are left unchanged with respect to the pre-industrial reference. To cover the most likely range of atmospheric greenhouse gases during the middle-to-late Eocene (~ 500 – 1200 ppm; Beerling and Royer 2011; Anagnostou et al. 2016; <http://www.p-co2.org>), as well
135 as to estimate climate sensitivity, a $2\times$ PIC and $4\times$ PIC simulation were carried out. CO_2 and CH_4



Property \ Case	Pre-industrial	38Ma 2× PIC	38Ma 4× PIC
Geography	Present day	38Ma Paleomag (Baatsen et al., 2016)	
Vegetation	Present day	38Ma; plant functional types fixed	
Aerosols	Pre-industrial	from 50-year BAM run	
CO ₂	280ppm	560ppm	1120ppm
CH ₄	671ppb	1342ppb	2684ppb
Spin-up	3100 years	3600 years	4600 years

Table 1. Overview of characteristics for all CESM 1.0.5 simulations that were performed (BAM: bulk aerosol model).

concentrations are increased simultaneously, in order to represent middle-to-late Eocene estimates (Beerling et al., 2009, 2011; Goldner et al., 2014). According to Etminan et al. (2016) the radiative forcing of 2× PIC and 4× PIC is equivalent to that of 2.15× CO₂ and 4.69× CO₂, respectively. Since the model simulations are designed to reconstruct the average climate over longer periods in

140 time (4–8 Ma), there is not a constant set of orbital parameters that is representative for the entire considered time interval. A set of parameters generally conducive for Antarctic ice growth is chosen: minimum eccentricity (i.e. 0; cancelling the effect of precession) and present-day obliquity (23.44°). The low eccentricity choice is motivated by the conjunction of two such minima occurring around the EOT, as shown by Coxall et al. (2005); DeConto et al. (2008). The solar constant was only

145 slightly lower (~0.3%) during the late Eocene and is therefore kept at its present-day value. The Eocene simulations both use the 38Ma geography reconstruction (Figure 1b,d) from Baatsen et al. (2016), which in contrast to most previously used geographies is based on a palaeomagnetic (‘PaleoMag’) reference frame. This method prioritises on the reconstruction of exact palaeolatitudes, crucial for palaeoclimate simulations (van Hinsbergen et al., 2015). As for any other ge-

150 ography reconstruction, it comes with its own limitations and uncertainties (Baatsen et al., 2016). The middle-to-late Eocene vegetation used here (Figure 1c) is largely based on Sewall et al. (2000) and comparable to the early Eocene vegetation of Herold et al. (2014). The mostly zonal bands in Sewall et al. (2000) are adjusted to the new geography reconstruction and likely marine influences. This translates into most of the earth being covered by various types of forests and shrubs (tropical

155 forest or savannah at low and mixed forests at middle-high latitudes). Neither desert regions, nor any land ice coverage are incorporated, while elevated surfaces are covered with a separate biome. Despite being an important contribution to the radiative forcing in present and future climate simulations, atmospheric aerosols are tricky to include and are therefore often either omitted or assumed to be similar to pre-industrial in palaeoclimate model simulations. A big improvement can be made

160 by running a Bulk Aerosol Model (BAM, Heavens et al. 2012) version of the CAM4 to determine a more realistic distribution of aerosols. The sources of naturally formed aerosols (mainly dust, sea



salt and organic carbon, excluding volcanic emissions) are adjusted from pre-industrial levels and redistributed based on the new land surface properties. Using these sources the (standalone) CAM4 is run for 50 years, at the end of which a monthly climatology of aerosol distributions is derived. An overview of the different model cases analysed in this paper is given in Table 1.

2.3 Spin-up procedure

Our 38Ma Eocene simulations are both initialised using a stagnant ocean with a horizontally homogeneous temperature distribution. The initial ocean temperature decreases with depth, from 15°C at the surface to 9°C at the bottom. The pre-industrial reference is initialised using temperature and salinity fields from the PHC2 dataset (Steele et al., 2001). A long spin-up (see Table 1) is performed to allow the deep ocean to equilibrate sufficiently. An overview of absolute (ΔT , ΔS) and normalised ($\Delta T/T$, $\Delta S/S$) drifts over the last 200 model years is given in Table 2 for each spin-up. Drifts are generally $\sim 10^{-5}$ – 10^{-4} K/year for global mean, volume weighted ocean temperature (values of $< 10^{-4}$ are often regarded as well equilibrated, see e.g. Goldner et al. 2014; Hutchinson et al. 2018). Similarly, for globally averaged salinity drifts at the end of the spin-up are $\sim 10^{-7}$ psu/year.

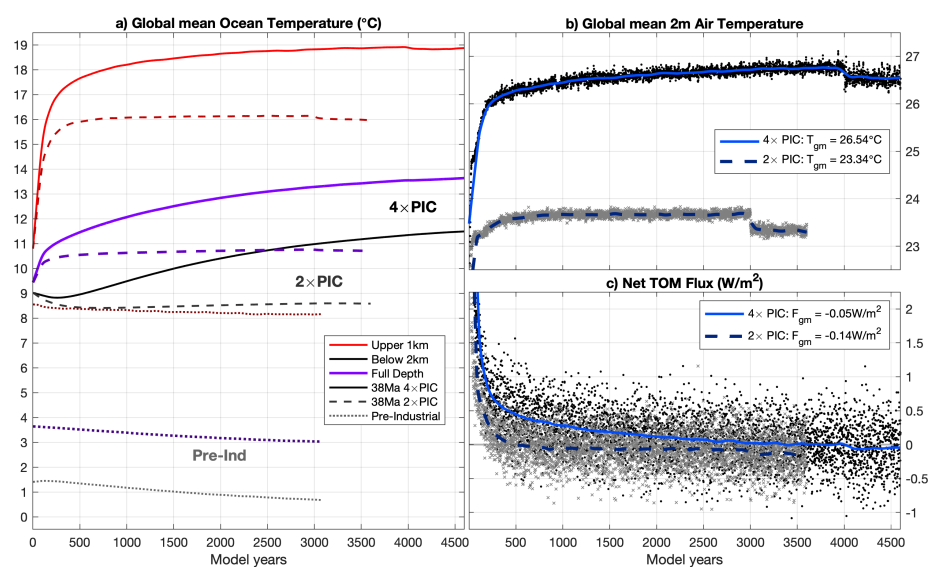


Figure 2. a) Time series of global upper 1km (red), below 2km (black) and full depth (purple) volume-weighted average temperature for the complete pre-industrial reference (dotted), 38Ma 2x PIC (dashed) and 4x PIC (solid) spin-up simulations. b) Global mean near surface air temperature for the 38Ma cases (markers: annual–grey crosses: 2x PIC, black dots: 4x PIC, lines: smoothed–dashed dark blue: 2x PIC, solid light blue: 4x PIC), with the average over the last 200 years given. c) Globally integrated top of model net fluxes for both 38Ma Eocene cases, using the same marker and line conventions as in b.



Time series of globally averaged upper (<1km), deep (>2km) and full depth ocean temperatures are shown for all three spin-up runs in Figure 2a. Starting from present-day initial conditions, the pre-industrial simulation cools down by about 0.5°C globally. The 38Ma 2× PIC simulation is seen to equilibrate much faster than the 4× PIC one, probably because the deep ocean equilibrium temperature is close to that of the initial state (~9°C). With higher greenhouse gas concentrations, the ocean experiences additional heating at the surface, causing it to become more strongly stratified which consequently reduces vertical mixing into the deep ocean. This reduced mixing in the 4× PIC case causes the global mean deep ocean temperature to still increase about 0.1°C over the last 500 years.

180
 185 As expected, changes in the upper 1km temperatures settle more quickly and are small (~0.1°C) for the last 2000 model years of each simulation.

Although generally adjusting more quickly than the ocean, near surface air temperatures can also be seen to equilibrate faster in the 38Ma 2× PIC case compared to the 4× PIC one. A small but abrupt temperature drop is seen at model years 3000 and 4000 for the 2× PIC and 4× PIC case, respectively. This is caused by a regional shift in vegetation cover that was necessary to adjust regions of initially switched PFTs in the Eocene boundary conditions. Since most of the land surface is covered with different types of forrest and the complexity of interactions with the modelled climate system is limited, the overall effect is minor. Both 38Ma simulations were extended by another 600 years, showing little change after a quick initial adjustment. Correcting the vegetation cover mainly affects the albedo, lowering the net fluxes at the top of the model atmosphere (Figure 2c). Time series of these fluxes also indicate that the atmosphere is close to radiative equilibrium for the most part of both simulations, with generally a ~0.1W/m² difference between globally integrated shortwave and longwave fluxes. This radiative balance agrees with the deep ocean continuing to warm up slightly while both the upper ocean and atmosphere show little change after model year ~1500 for the 38Ma

190
 195
 200 4× PIC simulation.

Measure	Simulation		
	Pre-industrial	38Ma 2× PIC	38Ma 4× PIC
ΔT (K/year)	$-8.7 \cdot 10^{-5}$	$-2.6 \cdot 10^{-5}$	$1.9 \cdot 10^{-4}$
ΔS (psu/year)	$-2.2 \cdot 10^{-7}$	$2.0 \cdot 10^{-7}$	$-2.9 \cdot 10^{-7}$
$\Delta T/T$ (/year)	$-3.2 \cdot 10^{-7}$	$-9.1 \cdot 10^{-8}$	$6.5 \cdot 10^{-7}$
$\Delta S/S$ (/year)	$-6.2 \cdot 10^{-9}$	$5.6 \cdot 10^{-9}$	$-8.2 \cdot 10^{-9}$

Table 2. Overview of drifts in global mean ocean temperature and salinity over the last 200 model years for all three CESM spin-up simulations. Normalised drifts $\Delta T/T$ and $\Delta S/S$, with T temperature in Kelvin and S salinity in psu, are also shown for each case using the same model period.



In addition, global patterns of ideal age tracers (a measure for oceanic ventilation timescales; Thiele and Sarmiento 1990; England 1995) are observed to equilibrate over the last 1000 years of each simulation (Supplementary Figure S1) as well as the meridional overturning strength and
205 oceanic gateway transports (Supplementary Figure S2). Average values of ideal age still have considerable trends because of further ageing in stagnant deep ocean regions (Figure S1a) and upwelling of older water masses into the upper ocean (Figure S1b). Such changes will likely continue for many thousands of years, but the associated circulation pattern has equilibrated by the end of each simulation, which is used for further analysis. The difference in spin-up between both 38Ma cases is once
210 again highlighted in the evolution of maximum overturning strength. Whereas the $2\times$ PIC simulation has a stable southern overturning cell within 500 model years, its equivalent in the $4\times$ PIC case only materialises after 2750 years (Figure S2b).

2.4 Proxy compilations

The 38Ma CESM simulations presented here are validated using both qualitative and quantitative
215 measures based on proxy records of the middle-to-late Eocene. After a general assessment of the model results we look more specifically at SSTs, where those from the 38Ma $4\times$ PIC simulation are assumed to best represent the 42–38 Ma proxy records, and from the $2\times$ PIC case for the 38–34 Ma interval. An overview of the considered SST proxies is given in Table S2 for 42–38 Ma and S3 for 38–34 Ma, using data from Pearson et al. (2001, 2007); Tripathi et al. (2003); Kobashi et al.
220 (2004); Bijl et al. (2009); Liu et al. (2009); Okafor et al. (2009); Douglas et al. (2014); Hines et al. (2017); Cramwinckel et al. (2018); Evans et al. (2018). A point-by-point comparison with proxy records is made, using their estimated 38Ma positions in accordance with the PaleoMag geography from Baatsen et al. (2016). Proxy-derived values for annual mean temperatures are considered with their calibration uncertainty for different methods (UK_{37} , TEX_{86}^H , Mg/Ca, Δ_{47} and $\delta^{18}O$). Modelled
225 SSTs at the reconstructed proxy locations are given with error bars representing the variance in a surrounding $4^\circ\times 4^\circ$ box, covering the uncertainty associated with the palaeogeographic reconstruction (<http://www.paleolatitude.org>). Estimates using UK_{37} are disregarded at low latitudes as the calibration saturates at $\sim 28^\circ C$ (Conte et al., 2006). There is an ongoing discussion on which calibration to use for TEX_{86} (O'Brien et al., 2017; Cramwinckel et al., 2018; Hollis et al., 2019). In addition to
230 SST estimates using the exponential TEX_{86}^H calibration from Kim et al. (2010), we show those using the linear relation of Kim et al. (2008) (light blue markers in Figure 6). There is also uncertainty in the calibration of Mg/Ca, for which we use the constraints on sea water chemistry from Evans et al. (2018).

In addition to SSTs, we compare modelled near surface air temperatures to terrestrial proxies. Simi-
235 larly, the distinction is made between the late middle Eocene (~ 42 –38 Ma) and late Eocene (~ 38 –34 Ma) as a reference for the 38Ma $4\times$ PIC and $2\times$ PIC simulations, respectively. The considered records are listed in Tables S4 and S5; containing data from Greenwood and Wing 1995; Gregory-



Wodzicki 1997; Smith et al. 1998; Wolfe et al. 1998; Greenwood et al. 2004; Retallack et al. 2004; Hinojosa and Villagrán 2005; Uhl et al. 2007; Boyle et al. 2008; Schouten et al. 2008; Prothero
240 2008; Eldrett et al. 2009; Quan et al. 2012; Passchier et al. 2013). Terrestrial proxies used here consist of vegetation-based indicators using pollen, nearest living relative (NLR), leaf physiognomy (LMA, CLAMP, ELPA and LMA; Wing and Greenwood 1993; Yang et al. 2011; Traiser et al. 2005; Kowalski and Dilcher 2003) and MBT-CBT (Peterse et al., 2012).

2.5 Previous model results

245 The results of our 38Ma simulations are compared to those of Goldner et al. (2014) (hereafter: GH14) and Hutchinson et al. (2018) (H18). We are mainly looking at zonally averaged sea surface and near surface air temperatures and how they correspond to the previously presented proxies. A side-by-side overview of oceanic and atmospheric fields from this study and GH14 can be found in the supplementary material.

250 The simulations of GH14 were carried out with the CCSM3, a predecessor of the CESM1 (the former having CAM3 with a spectral versus CAM4 with a finite volume core). GH14 used a 45Ma Hot Spot referenced reconstruction for their geographical boundary conditions, in which Antarctica is shifted by $\sim 6^\circ$ latitude compared to the 38Ma PaleoMag reconstruction used here. They applied 4 subsequent doublings of pre-industrial CO_2 levels, which correspond to the EO1–EO4 cases of
255 Cramwinckel et al. (2018). In terms of horizontal resolution GH14 implemented $\sim 2.5^\circ$ and 3.7° for the model's ocean and atmosphere grids, respectively, versus $\sim 1^\circ$ and $\sim 2^\circ$ here.

A model set-up similar to ours was implemented by H18, using the 38Ma geography reconstruction from Baatsen et al. (2016) and a similar oceanic resolution ($\sim 1^\circ$ – atmosphere: $\sim 3^\circ$). They studied mostly the late Eocene, but using the GFDL CM2.1 rather than the CESM and subsequent doublings
260 of present-day CO_2 concentrations (i.e. $\sim 400\text{ppm}$).

A more quantitative assessment of the model's performances is made following a procedure similar to the one presented by Lunt et al. (2012), using the SST proxy compilations (Tables S2 and S3). The model-proxy discrepancy σ is defined as the average difference between model-predicted and proxy-induced SSTs at reconstructed locations (using 38Ma PaleoMag for this study and H18 versus 45Ma
265 HotSpot for GH14). A set of different comparisons is considered, using either all proxies or a subset and modelled annual mean versus summertime temperatures. An *absolute* error $|\sigma|$ is also introduced (rather than e.g. RMS) to rule out better scores by compensating errors without exaggerating the impact of a single (possibly unrealistic or not representative) proxy value.

2.6 Climate sensitivity

270 A number of additional simulations are carried out to determine the model's response to an altered radiative forcing when only the concentration of atmospheric greenhouse gases is changed. These include a 500-year $4\times \text{CO}_2$ (Figure S15), and four 20-year perturbation experiments listed below.



Using the extrapolation method introduced by Gregory et al. (2004) on the results of those shorter simulations (see Figure S16 for $4\times\text{CO}_2$), the model-derived radiative forcing from consecutive doublings of either CO_2 or both CO_2 and CH_4 is determined as (bracketed values: theoretical estimates from Etminan et al. 2016; E16):

$$- 1\times\text{CO}_2 \rightarrow 2\times\text{CO}_2: \Delta\text{RF}^{2\times\text{CO}_2} = 3.49 \text{ W/m}^2 \text{ (E16: } 3.80 \text{ W/m}^2\text{)}.$$

$$- 1\times\text{CO}_2 \rightarrow 4\times\text{CO}_2: \Delta\text{RF}^{4\times\text{CO}_2} = 7.93 \text{ W/m}^2 \text{ (E16: } 7.96 \text{ W/m}^2\text{)}.$$

$$- 1\times\text{PIC} \rightarrow 2\times\text{PIC}: \Delta\text{RF}^{2\times} = 4.18 \text{ W/m}^2 \text{ (E16: } 4.23 \text{ W/m}^2\text{)}.$$

$$- 1\times\text{PIC} \rightarrow 4\times\text{PIC}: \Delta\text{RF}^{4\times} = 9.33 \text{ W/m}^2 \text{ (E16: } 8.96 \text{ W/m}^2\text{)}.$$

The value of $\Delta\text{RF}^{2\times\text{CO}_2}$ determined here is slightly lower than the 3.8W/m^2 estimated by E16, but very close to the 3.5W/m^2 reported by Kay et al. (2012) using offline radiative transfer calculations for CAM4 specifically. Note that the model-derived radiative forcing is generally close to the corresponding one from E16, but feature a stronger nonlinear behaviour towards higher perturbations especially when including the effect of CH_4 . Using the values shown above, the radiative forcing that results from a second PIC doubling can also be estimated as: $\Delta\text{RF}_{2\times}^{4\times} = 5.15\text{W/m}^2$ ($= \Delta\text{RF}^{4\times} - \Delta\text{RF}^{2\times}$). Through a (log scaled) quadratic fit, these estimates can also be used to show that our $2\times\text{PIC}$ is equivalent to $2.25\times\text{CO}_2$ while $4\times\text{PIC}$ corresponds to $4.85\times\text{CO}_2$ (rather than 2.15 and 4.69 based on E16, respectively).

Starting from the equilibrated pre-industrial reference (at model year ~ 3100), an instant quadrupling of atmospheric CO_2 was applied and continued for another 500 model years. Using the same procedure as Gregory et al. (2004), the equilibrium climate sensitivity (ECS) of the model was assessed at 3.14°C per CO_2 doubling (i.e. 6.28°C from $4\times\text{CO}_2$). The first 100 model years are disregarded in the extrapolation to better incorporate the effect of slow feedbacks (see Figure S15). Using the same atmospheric configuration and a slab ocean model, Bitz et al. (2012) also reported this response in the CCSM4. With the model-derived radiative forcing of 7.93 W/m^2 and an extrapolated equilibrium response of 6.28°C , the normalised equilibrium climate sensitivity of the pre-industrial reference is therefore: $S_{PI} = 0.79^\circ\text{C/Wm}^{-2}$.

Since we carry out a long spin-up simulation for each of the 38Ma cases, we can determine the equilibrium climate response as the difference between the actual equilibrium states rather than making an estimate through extrapolation. The average over the last 200 (rather than 50 for the other results) model years of each simulation is taken to exclude as much of the internal variability as possible. When comparing global mean temperature differences between the pre-industrial reference and both Eocene simulations, not all of the warming is a result of higher greenhouse gas concentrations. To separate the *internal* effect of palaeogeography from the *externally* (i.e. greenhouse gas) driven warming, the 38Ma Eocene equilibrium climate sensitivity S_{EO} can also be calculated using



the combined radiative forcing due to greenhouse gas and palaeogeography changes by assuming that:

$$310 \quad S_{EO} = \frac{\Delta T}{\Delta RF + G}, \quad (1)$$

where ΔT is the temperature difference between two climatic states, ΔRF the net radiative forcing from greenhouse gases and G the radiative forcing due to the (integral) effect of palaeogeography. Note that the latter also includes changes in the distribution of e.g. land ice and vegetation, as those are external boundary conditions in the model set-up used here. In order to be compatible with S_{PI} ,

315 this formulation returns S in normalised units of [$^{\circ}\text{C}/\text{Wm}^{-2}$], rather than [$^{\circ}\text{C}$ per CO_2 doubling] as used by Royer et al. (2012).

Since both 38Ma Eocene simulations use the same (except CO_2 and CH_4) boundary conditions, it is reasonable to assume that S and G estimated from the comparison with the pre-industrial case should be similar (provided that their nonlinear contribution is small). By comparing the temperatures of

320 both Eocene runs to those of the pre-industrial reference, G can then be estimated from:

$$G = \frac{\Delta T^{2\times} \cdot \Delta RF^{4\times} - \Delta T^{4\times} \cdot \Delta RF^{2\times}}{\Delta T^{4\times} - \Delta T^{2\times}}, \quad (2)$$

where $\Delta T^{4\times}$ and $\Delta T^{2\times}$ denote the temperature difference with respect to the pre-industrial climate for the 38Ma $4\times$ PIC and $2\times$ PIC case, respectively. Within this formulation, globally averaged near surface air temperatures can be substituted by equatorial ($<23.5^{\circ}\text{N/S}$) SSTs (with a 3/2 ratio

325 between global and equatorial change suggested by Royer et al. 2012) or deep sea temperatures, which are both more compatible with ECS estimates from proxy data.



3 Results

3.1 The simulated middle-to-late Eocene equilibrium climate

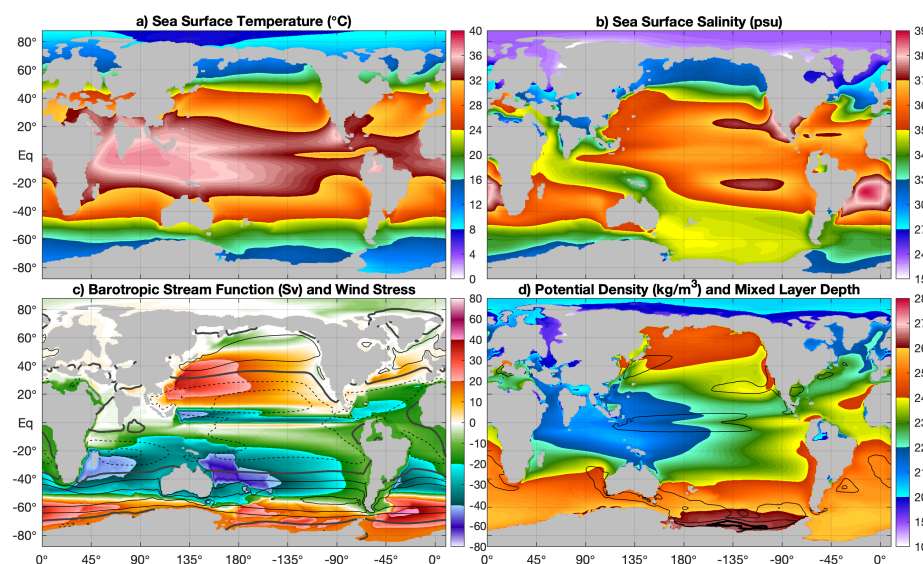


Figure 3. Annual mean **a)** sea surface temperature and **b)** salinity, **c)** barotropic stream function (positive for clockwise flow) and zonal wind stress (contours every $5 \cdot 10^{-2}$ Pa, solid positive and dashed negative, thick line at 0 Pa), and **d)** upper 200m mean potential density and mixed layer depth (contours at 100m and 200m, thick line at 500m) for the $4 \times$ PIC simulation.

Taking the average of the last 50 years of the 38Ma $4 \times$ PIC simulation, a number of annual mean
330 oceanic fields are shown in Figure 3 (see also Figure S3 for the pre-industrial reference and Figure
and S4 for the 38Ma $2 \times$ PIC case, seasonal fields are shown in figure S7). Sea surface temper-
atures are quite warm at low latitudes (34°C on average, regionally $>36^\circ\text{C}$) but also mild across
high latitudes (Figure 3a). Mainly the Southern Ocean and especially its Pacific part is characterised
by annual mean temperatures of $10\text{--}20^\circ\text{C}$, while those of the Arctic Ocean are mostly $6\text{--}10^\circ\text{C}$.
335 The former NeoTethys (Pacific-Indian-Mediterranean) Ocean still mostly acts as one basin in the
equatorial region, with an expansive warm pool and cold tongue across its western and eastern part,
respectively.

Mild temperatures in the sub-polar South Pacific are accompanied by relatively high salinities of
around 35psu (Figure 3b). Higher salinities are present across low latitude evaporative regions
340 around the world, in contrast to the much fresher Arctic Ocean (~ 20 psu). The latter is geographi-
cally almost isolated, only connected to the shallow Paratethys by the Turgai Strait (<100 m depth)
and through the Nordic Seas (<1 km depth) to the North Atlantic Ocean where consequently low



surface salinities are seen as well.

The surface temperature and salinity patterns are reflected by upper 200m potential density (Figure 3d), with high values throughout the Southern Ocean and much lower densities and thus more stably stratified waters across the North Atlantic and Arctic Oceans. Deep water formation occurs only in the Pacific sector of the Southern Ocean in winter (at $\sim 11.4^{\circ}\text{C}$ and 34.8psu), but high upper level densities suggest that this may take place virtually anywhere around the Antarctic continental slope. The only part of the Northern Hemisphere where deep water formation could occur is the high latitude Pacific Ocean, but is never seen in either of the 38Ma simulations).

The global ocean circulation consists mostly of expansive sub-tropical gyres a geographically restricted Antarctic Circumpolar Current (ACC) and some rather weak sub-polar gyres (Figure 3c). The ACC is associated with a rather sharp frontal zone separating warm sub-tropical from cooler sub-polar waters. Despite its strongly restricted path by the Drake Passage and Tasmanian Gateway (200–500 m; see Figure 1a,d), the integrated zonal flow is about 25–30 % of its pre-industrial equivalent (45–50 Sv vs 180Sv; see also Figure S2a). Strikingly, the temperature front is located at $55\text{--}60^{\circ}\text{S}$, which is almost 10° poleward of where it is found in the pre-industrial reference (Figure S3). The zonal variability in the location of the front also has profound implications on regional meridional temperature contrasts. This location is strongly bound by the zonal wind stress maximum, indicating that it is fixed by the latitudes where both atmospheric and oceanic flow are the least obstructed by continents.

Measure	Simulation		
	Pre-industrial	38Ma 2× PIC	38Ma 4× PIC
MAT_{glob} ($^{\circ}\text{C}$)	13.82	23.34	26.55
SST_{glob} ($^{\circ}\text{C}$)	18.41	25.68	28.32
SST_{eq} ($^{\circ}\text{C}$)	26.91	31.63	34.00
T_{deep} ($^{\circ}\text{C}$)	0.69	8.59	11.47

Table 3. Average equilibrium temperatures over the last 200 model years of each simulation, showing MAT_{glob} : global mean air temperature (at 2m reference height), SST_{glob} : global mean sea surface temperature, SST_{eq} : equatorial ($<23.5^{\circ}\text{N/S}$) average SST, and T_{deep} : global mean deep ocean ocean temperature (below 2km).

Despite differences in spin-up time, patterns of the equilibrium ocean circulation state are generally similar for our 38Ma 2× PIC and 4× PIC simulations (see also Figure S4). The annual mean, global mean sea surface temperature (SST) is 28.4°C in the 4× PIC case versus 25.7°C in the 2× PIC one and 18.4°C in the pre-industrial reference (Table 3). Similar temperature differences of $2.5\text{--}3^{\circ}\text{C}$ between are seen in both the upper and deep ocean between the 38Ma cases (Figure 2a). Globally averaged deep-sea temperatures (below 2km) reach $\sim 11.5^{\circ}\text{C}$ in the 38Ma 4× PIC case and $\sim 8.6^{\circ}\text{C}$ in the 2× PIC one, which is much warmer than for the pre-industrial ocean ($\sim 0.7^{\circ}\text{C}$). The differ-



370 ence in equatorial ($<23.5^{\circ}\text{N/S}$) SSTs between the Eocene cases and the pre-industrial reference is smaller, but still considerable.

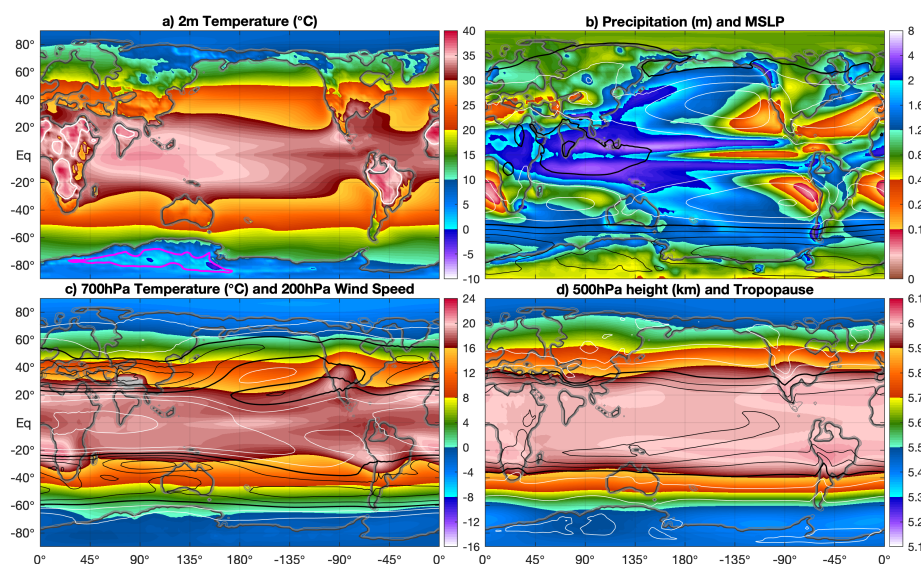


Figure 4. Annual mean for the $4\times$ PIC simulation with **a)** near surface (2m) air temperature (shading) and average min/max temperature (contours; magenta for $T_{min} < 0^{\circ}\text{C}$ and white for $T_{max} > 40^{\circ}\text{C}$), **b)** precipitation (shading) and mean sea level pressure (contours every 5hPa, thick black lines every 20hPa, $\leq 1000\text{hPa}$ in black and $> 1000\text{hPa}$ in white), **c)** 700hPa temperature (shading) and 200hPa wind speed (contours every 5m/s starting at 10m/s; white for $< 20\text{m/s}$ and black for $> 20\text{m/s}$, thick black lines every 20m/s), and **d)** 500hPa geopotential height (shading) and tropopause height (contours every 1km starting at 12km; white for $< 15\text{km}$ and black for $> 15\text{km}$, thick black line at 15km).

Again averaging over the last 50 years of the 38Ma $4\times$ PIC simulation, annual mean atmospheric fields are shown in Figure 4 (see also Figure S5 for the pre-industrial reference and Figure and S6
375 for the 38Ma $2\times$ PIC case, seasonal fields are shown in figure S8). The modelled Eocene climate is overall warmer and wetter than that of the pre-industrial reference, with reduced contrasts between low and high latitudes. Near surface air temperatures (at 2m; Figure 4a) under $4\times$ PIC are above zero and up to 40°C over land at low latitudes in the annual mean (with summer maxima regionally $> 50^{\circ}\text{C}$; see Figure S8a,b). Annually averaged (daily) minimum temperatures are only below freeze-
380 ing in East Antarctica and Northeast Siberia. Extreme seasonality is seen over the continental interior of Antarctica, with $35\text{--}45^{\circ}\text{C}$ differences between daily mean summer and winter temperatures. Simulated precipitation and mean sea level pressure (MSLP) patterns (Figure 4b) indicate the presence of a prominent tropical trough and expansive sub-tropical ridges in the Eocene. The inter-



tropical convergence zone (ITCZ) consists of 2 precipitation maxima, extending over the Indo-
385 Pacific basin on both sides of the equator. A pronounced double ITCZ over the Pacific Ocean is also
seen in the pre-industrial reference (Figure S5b) and a known model-related issue (Song and Zhang,
2009; Bellucci et al., 2010). Effects of orographic lift are evident on westward facing coastlines and
mountain ranges across middle and high latitudes. Regardless of an overall reduced equator-to-pole
temperature gradient in the 38Ma 4× PIC case, middle latitude storm tracks are prominent with in-
390 creased precipitation and a poleward expansion with respect to the pre-industrial reference. Strong
seasonality in the precipitation patterns also indicates the importance of monsoons in this warm
Eocene climate (Figure S8c,d).

The modelled 700hPa temperature (Figure 4c) of the 38Ma 4× PIC case highlights warm mid-level
air masses in persistent continental high pressure regions in the sub-tropics. The air over Antarctica
395 is substantially warmer than over the Arctic because of its elevation and continental climate. Like
the Tibetan Plateau today, the Antarctic continent therefore acts as an elevated heat island in sum-
mer (Hoskins and Karoly 1981; Ye and Wu 1998; Figure S8f). Wind speeds at 200hPa highlight the
positions of both sub-tropical and polar jet streams. Several wind maxima, related to (mostly topo-
graphically induced) preferred Rossby Wave activity are evident but most pronounced at ~90°E. A
400 mostly similar jet stream pattern with regional wind maxima is seen in the pre-industrial reference,
but shifted poleward and more zonally uniform.

Reduced latitudinal as well as hemispheric differences in the modelled 38Ma 4× PIC compared to
the pre-industrial reference are also seen in 500hPa geopotential and tropopause heights (Figure 4d).
The latter is defined using the WMO definition of -2°C/km lapse rate. Both fields show a nearly
405 meridionally symmetric pattern for the Eocene, with the sharpest gradient across middle-latitude
regions. The overall warmer air column in the Eocene case accounts for an increase of the 500hPa
surface by 100-200 m (up to 400m over Antarctica) and tropopause by 1–2 km. The 500hPa surface
is generally about 200m higher than in the pre-industrial reference, mainly due to warming of the air
column.

410 As for the ocean, the modelled 38Ma 2× PIC atmosphere (Figure S6) looks quite similar to the
4× PIC one. At 23.34°C the globally averaged, annual mean near surface air temperature at 2× PIC
is ~3.2°C cooler than at 4× PIC (26.55°C). This is, however, still ~9.5°C warmer than in the prein-
dustrial reference (13.82°C).

415 The global heat budget in the modelled results is assessed by looking at both the oceanic and at-
mospheric heat fluxes, as well as their link to global circulation patterns, presented in Figure 5. The
globally integrated oceanic meridional overturning stream function is similar in pattern and extent
(Figure 5a) for both 38Ma Eocene simulations. Shallow wind driven cells are evident around the
equator and a deep overturning cell is present in the Southern Hemisphere, which is slightly stronger
420 in the 2× PIC case. The effect of upwelling by zonal flow in the ACC can be seen at around 55°S in

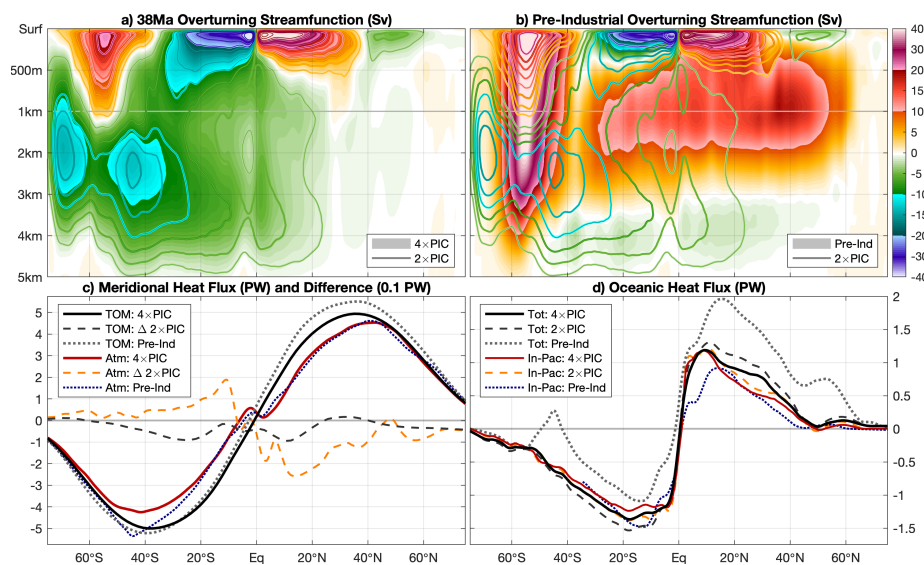


Figure 5. Global oceanic meridional overturning stream function, averaged over the last 50 model years of the **a)** 38Ma 4 × PIC (shading) and 2 × PIC (contours) Eocene simulations, and **b)** pre-industrial reference (shading; 38Ma 2 × PIC again in contours). Contours are drawn at ± 2.5 Sv and every 5 Sv onward, using the same colourmap shown at the right side. Top of model (TOM) required total meridional heat flux is shown in **c)** for 4 × PIC (solid black) and the pre-industrial reference (dotted grey) with the corresponding atmospheric fluxes in red (4 × PIC) and dotted blue (pre-industrial). Differences with respect to 38Ma 4 × PIC of both total (dashed dark grey) and atmospheric (dashed orange) heat flux are given for the 2 × PIC case, magnified tenfold. **d)** Total integrated meridional heat fluxes in the ocean, globally and Indo-Pacific only, using the same colour coding as in **c)** for TOM and atmosphere, respectively. Note that all horizontal (latitude) scales cover the range $[75^{\circ}\text{S}, 75^{\circ}\text{N}]$ with latitude increasing from left to right, for better comparison with oceanic fields in **a)** and **b)**.

both 38Ma cases as well as the pre-industrial reference. The latter is much deeper and stronger as a result of a stronger ACC but mostly the unrestricted zonal flow in the present geographical configuration. Note that the average latitudinal shift of these overturning cells between the modelled Eocene and pre-industrial circulation is less pronounced than the more regional variations of the surface polar front in Figures 3 and S3.

425

An otherwise predominantly wind-driven gyre circulation is reflected by symmetric oceanic meridional heat fluxes into both hemispheres (Figures 5d). This is in contrast to the pre-industrial situation, where a difference of up to 1PW is seen between hemispheres, making the Northern Hemisphere relatively warm (Trenberth and Caron, 2001). A major part of the oceanic heat flux occurs in the Neotethys/Indo-Pacific Ocean, indicating its dominant role within the Eocene circulation. The presence of a deep overturning cell in the North Atlantic Ocean in the pre-industrial reference substantially reduces the relative Ind-Pacific contribution.

430



A subtle but important difference between hemispheres is seen at high latitudes, where about 0.5PW is transported southward at 45°S while the heat transport is close to zero at 45°N in both 38Ma cases.

435 This difference can be explained by the presence of a deep meridional overturning cell in the South Pacific, pulling warm waters into the southern high latitudes.

To determine the total required meridional heat flux, top of model net fluxes are integrated zonally (Figure 5c). Overall differences are small between the 38Ma cases and pre-industrial reference, with a slight shift towards the Southern Hemisphere making the Eocene pattern more symmetric. Changes

440 in oceanic meridional heat fluxes are less pronounced in the total flux and are thus compensated by the atmospheric component, albeit only partially. The reduced latitudinal temperature gradients seen in the modelled 38Ma cases are not sustained by increased meridional heat fluxes, but rather induce reduced fluxes with respect to to the pre-industrial reference.



445 3.2 Model-proxy comparisons

In terms of the general ocean circulation, proxy-based information is limited but mostly agrees well with what is shown by the model. Persistent deep water formation in the South Pacific Ocean throughout most of the Eocene and the possibility of a North Pacific or South Atlantic source are consistent with the findings of (Cramer et al., 2009; Hague et al., 2012). A strongly stratified North
450 Atlantic Ocean with low salinity waters at middle-high latitudes was also suggested by Coxall et al. (2018), prior to ~36Ma.

The all but complete absence of Arctic sea ice in the 38Ma 4× PIC model results differs from indications of seasonal sea ice during the middle Eocene by Stickley et al. (2009). Although limited in extent, the model does show sea ice during the winter months under 2× PIC (contours in Figure
455 S4). In addition to the sea ice indications being highly localised, age restrictions on the considered section of the ACEX core make it difficult to rule out whether the sea ice actually occurred in the late Eocene. Still, the model's limitations to represent sea ice need to be considered here, as the applied scheme is quite simple. Low salinities across the Arctic Ocean would have made it easier for sea ice to form, which is not reflected by the implemented fixed SST threshold (-1.8°C).

460 A southward migration of the temperature front in the Southern Ocean can help to explain some of the high SSTs induced from proxies, especially across the Southwest Pacific region (Bijl et al., 2009; Hines et al., 2017). Additionally, zonal variations in the front induce a thermal heterogeneity in the Southern Ocean. The 6–8 °C (Figure 3a) difference between Tasmania and the tip of the Antarctic Peninsula (Seymour Island) agree well with proxy indications from Douglas et al. (2014).
465 On the other hand, eastward flow through the Tasmanian Gateway limits the strength and extent of the Antarctic counter current around most of Antarctica (Bijl et al., 2013; Houben et al., 2019). The model results disagree with indications of a strong sub-polar gyre in the Ross Sea into the late Eocene, with predominantly westward flow through the Tasmanian Gateway and Antarctic-derived surface waters found in the Southwest Pacific Ocean (Stickley et al., 2004; Huber et al., 2004; Bijl
470 et al., 2013; Cramwinckel et al., 2019). The absence of a clear temperature discrepancy between both sides of the gateway still suggests a strong connection as seen in the model (Bijl et al., 2013), possibly explained by atmospheric influences at shallow and near-coastal locations.

In Figure 6 a point-by-point comparison with the available proxies (dots) is complemented with
475 zonally averaged SSTs from the model (solid line) along with their longitudinal spread (shading) for both the annual mean (black) and summer (red) average (for 38Ma 4× PIC, see also Figure S9 for 2× PIC).

For low-latitude regions, model results and proxies are generally in good agreement (i.e. within uncertainty). Some near-equatorial sites (e.g. Atlantic ODP Sites 925, 929 and 959) show cooler
480 temperatures than suggested by the model, at around 30°C (when considering TEX_{86}^H). Both the model's limitations representing the sharp upwelling region and uncertainty in the palaeolatitude

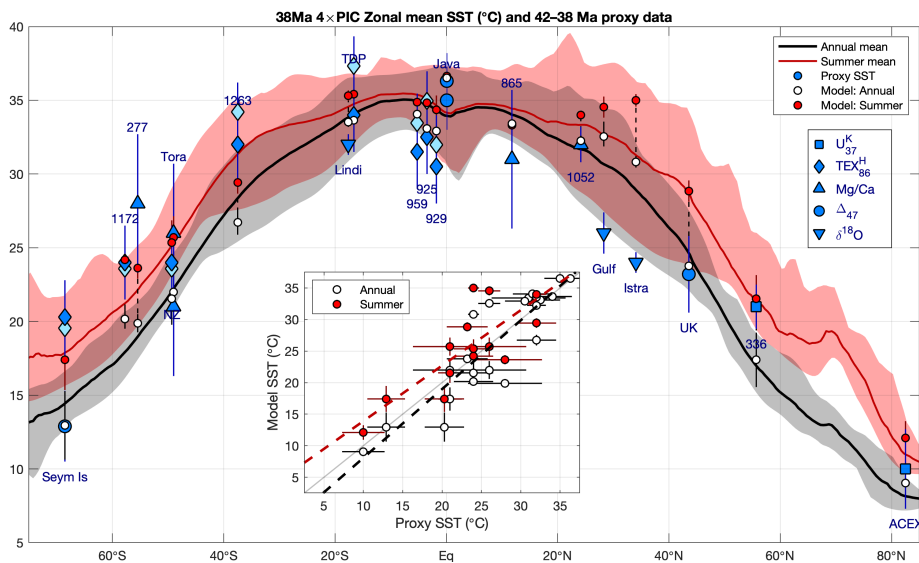


Figure 6. Zonal mean, annual mean (black) and summer mean (red) sea surface temperature (SST) with shaded regions showing minimum and maximum values for each latitude (38Ma 4 × PIC simulation). Blue markers indicate estimates from 42–38 Ma SST proxies (light blue: linear, dark: log calibration from citealtKim2008), whereas the white (annual) and red (summer) circles depict model values at the corresponding 38Ma locations. Error bars are obtained using proxy calibration errors and the spatial variation within a 4° × 4° box surrounding the corresponding location in the model. The inset shows a scatter plot comparing proxy and model SST, with dashed lines indicating a linear fit using annual mean (black) or summer mean (red; only poleward of 23°N/S) model temperatures.

can explain this offset. Cooler near-equatorial temperatures (down to <30°C) are in fact indicated by the increased zonal spread, showing that these are possible in the simulated Eocene climate. TEX₈₆^H estimates from Tanzania and recent clumped isotope measurements from Java suggest that
 485 SSTs of ~35°C or more are possible outside of upwelling regions, which is well in line with the 38Ma 4 × PIC results.

A mixed agreement is seen at other latitudes, with model results seemingly too warm at northern middle latitudes, too cold at southern middle latitudes and good at high latitudes. The large discrepancy with proxy estimates from the Gulf of Mexico and Neotethys (Mediterranean) stands out.
 490 While it seems unlikely that these regions would be colder in the Eocene than they are today, the model probably underestimates strong seasonal cooling in shallow coastal waters and other localised effects near the coastline due to the complex palaeogeography at both locations. SST estimates from other locations at a similar latitude, such as ODP Site 1052 on Blake Nose (east of Florida) are much higher bringing them back into good agreement with the model.

495 An improved match is generally found at most southern middle and high southern latitudes when



modelled summertime temperatures are considered. Since SST proxies are based on past living organisms, they possibly have a bias towards the warm season as their activity and sedimentation are directly or indirectly affected by the available amount of sunlight (Sluijs et al., 2006, 2008; Bijl et al., 2009; Hollis et al., 2012; Schouten et al., 2013). Confidence in the modelled annual mean SSTs is boosted by a near perfect agreement in the Arctic and clumped isotope indicators elsewhere (UK and Seymour Island).

The modelled 38Ma $2\times$ PIC SSTs similarly show an overall good agreement with 38–34 Ma proxy estimates, with a higher spread in the latter (Figure S9 and Table S3). The best overlap is again seen in low latitude regions, as well as a better match with modelled summer temperatures at high latitudes (except for clumped isotopes). Considering the model's limitations and uncertainties or possible biases in proxy-derived SST estimates, these 38Ma simulations can reconstruct the middle-to-late Eocene (42–34 Ma) temperature distribution well.

Despite the limited latitudinal coverage of terrestrial proxies, an overall good agreement is also seen between the modelled temperatures on land and (Figure S10 for 38Ma $4\times$ PIC, see also Figure S11 for $2\times$ PIC). Proxy estimates from China, however, indicate little change in temperature while the model shows considerably warmer conditions at lower latitudes. Quan et al. (2012) discuss the limitations of capturing high summer temperatures, as it is unlikely to see similar conditions over a $>20^\circ$ latitude range. There are currently no proxy indications to assess the possibility of very high model-based temperatures (exceeding 50°C , see Figure S8a,b) in low latitude continental interiors. An important limitation of the model, especially on land, is its resolution which smoothens the topography and therefore underestimates local temperature effects. A correction using the original 0.1° geography reconstruction from Baatsen et al. (2016) and a free tropospheric lapse rate of -6.5K/km significantly improves the agreement between modelled and proxy-based temperatures, especially in North America (small squares versus filled markers in the inset of Figure S10).



3.3 Model-model comparisons

Zonally averaged SSTs of our 38Ma 4× PIC and 2× PIC simulations are compared to those of the 4× CO₂ (i.e. 1120ppm) case from GH14 and the 800ppm CO₂ (i.e. 2× PD) case from H18 in Figure 7, along with the pre-industrial reference and the available middle-to-late Eocene proxies. A similar overview considering near surface air temperatures and terrestrial proxies can be found in Figure 8. All of the Eocene cases feature an overall warming compared to the pre-industrial reference which is the strongest over southern high latitudes, along with a reduction of the equator-to-pole temperature gradient. Both of our 38Ma cases and the 800ppm simulation of H18 are considerably warmer than the 45Ma 4× CO₂ of GH14, indicating a higher sensitivity to the applied Eocene boundary conditions.

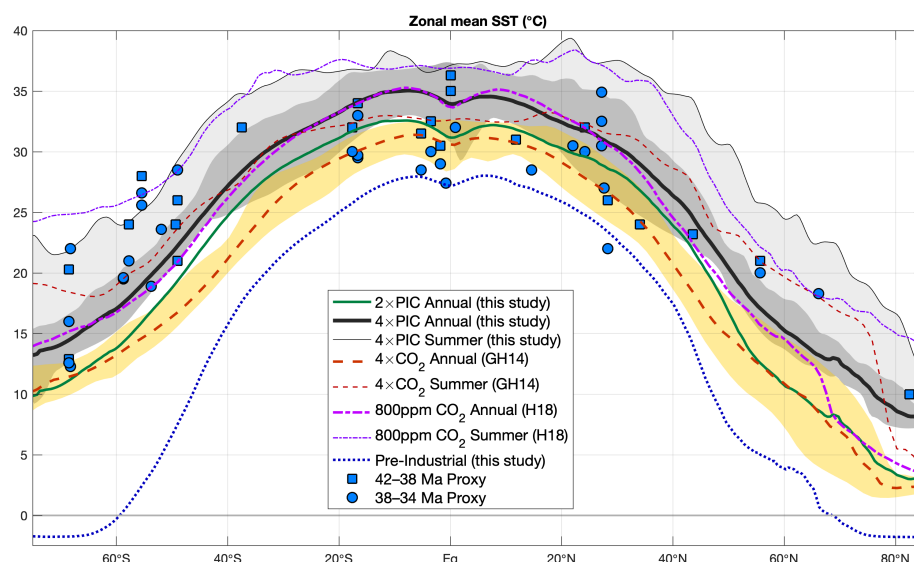


Figure 7. Annual mean, zonal mean sea surface temperature for the 38Ma 4× PIC (black; this study) and 2× PIC (dotted green; this study), 45Ma 4× CO₂ (dashed red; GH14 – Goldner et al. 2014), 38Ma 2× CO₂ (i.e. 800ppm, dash-dotted magenta; H18 – Hutchinson et al. 2018) and pre-industrial reference (dotted blue) simulations. Estimates from proxy data are represented by crosses for 42–38 Ma and circles for the 38–34 Ma period in accordance with other figures. Shading indicates the zonal range in temperatures for both the 38Ma 4× PIC (grey) and 45Ma 4× CO₂ (yellow) case, thin lines show the highest summer temperatures at each latitude (light grey shading added for 38Ma 4× PIC).

The most prominent differences in geography between the 45Ma and 38Ma simulations are the representation of Antarctica, the Tasmanian Gateway opening and the position of India. Especially the Southern Ocean shows large differences in circulation and the resulting temperatures, mainly related to the different model geographies. The formation of a proto-ACC and southern extent of the



535 East Australia current act to shift the polar front in the South Pacific southward for the 38Ma cases,
while the opposite happens for 45Ma (Figure S12). The southward expansion of sub-tropical gyres
and migration of the associated temperature front seen here is consistent with the findings of Viebahn
et al. (2016) in response to a Drake Passage closure under present-day conditions. These changes
can thus be linked directly to the continental configuration and associated shifts in zonal wind stress
540 (maximum at 55°S versus 45°S in GH14). Generally, western boundary currents (e.g. Kuroshio, Ag-
ulhas, East Australia Current) and the effects of ocean bathymetry are more pronounced in the 38Ma
results. An issue in the 45Ma results with very low (negative) salinities in the Arctic Ocean, although
having seemingly little impact on the general circulation, is mostly resolved (lowest salinities down
to ~10psu) in the 38Ma case by having several shallow passages.

545 With several indications of near-equatorial temperatures as high as 34–36 °C (Tanzania, Java and
Saint Stephens Quarry), the 38Ma 4× PIC case is able to match those proxies while still allow-
ing equatorial upwelling zones to be <30°C. The 800ppm CO₂ case of H18 shows similar tropical
warmth, but a steeper equator-to-pole temperature gradient especially in the Northern Hemisphere.
Cooler low-latitude proxies of ~30°C are better matched by both the 45Ma 4× CO₂ (GH14) and
550 38Ma 2× PIC results. Southern Hemisphere high latitude proxies are difficult to meet by any model
because of their large spread, with some of the higher estimates only matched by the warmest sum-
mertime temperatures in both the 38Ma 4× PIC and 800ppm CO₂ (H18) case. Still, most of the
lower estimates are best reconstructed by the annual mean SSTs in the 38Ma 4× PIC case while also
meeting the higher estimates when considering summer conditions.

555

Similar to the ocean results, all of the considered Eocene simulations show a comparable zonal
mean near surface air temperature distribution that differs greatly from the pre-industrial reference
(Figure 8). Extreme summertime heat over low/middle latitude continental regions is seen in our
38Ma 4× PIC cases, but also present in the 38Ma 2× CO₂ from H18 and to a lesser extent in the
560 45Ma 4× CO₂ from GH14. Part of this warmth can be explained by the use of fixed vegetation types
in all of the models, creating an efficient evaporative surface while most plants would otherwise
perish. The large seasonality over Antarctica is enhanced in our 38Ma simulations compared to both
GH14 and H18, with summer temperatures >30°C in the 4× PIC results (versus 20°C in GH14).
This Antarctic summertime warmth, together with cloud-albedo feedbacks over the Arctic keeps
565 annual mean, zonally averaged temperatures above 5°C in our 38Ma 4× PIC simulation across all
latitudes.

Global mean temperatures under similar radiative forcing are strongly model dependent for the
Eocene conditions studied here. While the 45Ma 4× CO₂ (GH14) case is cooler than our 38Ma
2× PIC one, H18 simulate conditions similar to those of our 4× PIC case at 800ppm CO₂ (albeit
570 with a steeper equator-to-pole temperature gradient). Although our 38Ma are the only ones with el-
evated CH₄ concentrations, the difference in global temperature is much larger than what would be

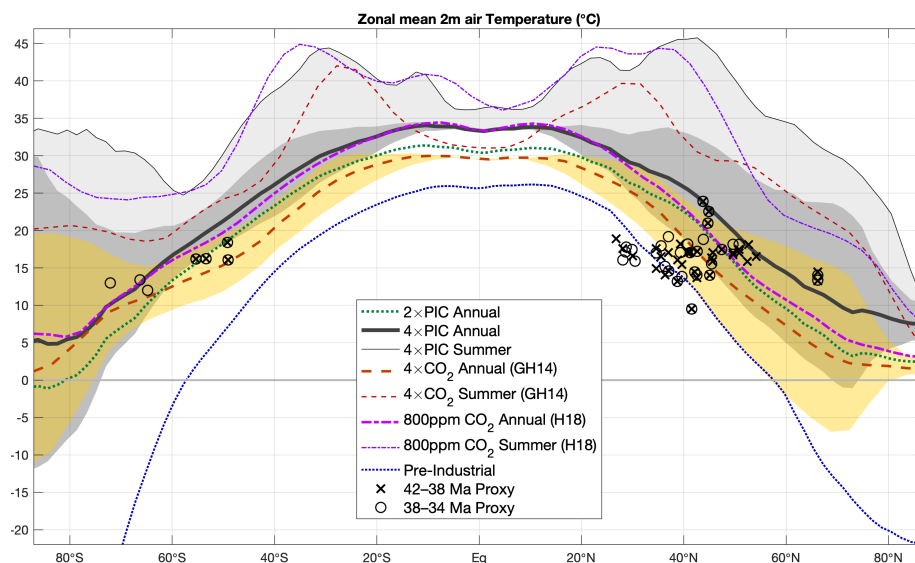


Figure 8. Annual mean, zonal mean near-surface (2m) air temperature for the 38Ma 4× PIC (black) and 2× PIC (dotted green), 45Ma 4× CO₂ (dashed red; GH14 – Goldner et al. 2014), 38Ma 2× CO₂ (i.e. 800ppm, dash-dotted magenta; H18 – Hutchinson et al. 2018) and pre-industrial reference (dotted blue) simulations. Estimates from proxy data are represented by crosses for 42–38 Ma and circles for the 38–34 Ma period in accordance with other figures. Shading indicates the seasonal (DJF, JJA) range in temperatures for both the 38Ma 4× PIC (grey) and 45Ma 4× CO₂ (yellow) case, thin lines show the highest summer temperatures at each latitude (light grey shading added for 38Ma 4× PIC).

expected solely from the resulting radiative forcing. The grid and resolution used here for the atmospheric component (CAM4) are shown to both increase the sensitivity to a doubling of CO₂ slightly (Bitz et al., 2012). Using the CAM4 finite volume dynamical core instead of a spectral one greatly
575 influences cloud radiative forcing and causes a warming compared to GH14 (There is a globally averaged net cloud forcing between the simulations of $13.8 - 6.4 = 7.4 \text{ W/m}^2$; see also Table S1). Indeed, similar global temperatures are found under comparable radiative forcing by H18, using a finite volume dynamical core.

Part of the temperature increase between pre-industrial and Eocene conditions can be explained by
580 the global land fraction being reduced from 29.2% to 26.2% in our CESM simulations. Lower land fraction generally reduces the earth's albedo and therefore induces a warming response as shown by Farnsworth et al. (2019). This cannot, however, explain the lower temperatures found by GH14, who implement a further reduced land fraction of 25.1% in their model boundary conditions. A warm
585 initialisation of the deep ocean, general circulation changes and the applied aerosol distribution add further to temperature differences between models. It is worth noting here that recent model results



from Zhu et al. (2019) also found a $\sim 5^\circ\text{C}$ warming in the CESM1.2 compared to their pre-industrial reference under the same external forcing, albeit for early Eocene (55Ma) conditions.

A more detailed comparison of the different components in the radiative balance between the considered simulations can be found in Table S1. The Eocene boundary conditions implemented here induce mainly a warming through the radiative forcing from greenhouse gases and a reduced albedo. The latter effect is mostly compensated by a negative cloud albedo feedback in GH14, but not in our 38Ma Eocene simulations. The warming is further enhanced by a strong positive water vapour feedback, explaining much the larger clear-sky longwave flux differences (i.e. 22.4W/m^2 globally) compared to what would be expected based on greenhouse gas concentrations alone.

595

Simulation	45Ma $4\times\text{CO}_2$ (GH14)	38Ma $2\times\text{CO}_2$ (H18)	38Ma $4\times\text{PIC}$ (this study)	38Ma $2\times\text{PIC}$ (this study)
σ_{glob} ($^\circ\text{C}$)	-4.81	-0.91	-0.43	-2.49
σ_{eq} ($^\circ\text{C}$)	-1.91	+1.83	+1.36	+0.82
σ_{ex} ($^\circ\text{C}$)	-6.47	-2.48	-1.45	-4.31
σ_{sum} ($^\circ\text{C}$)	(-2.86) -2.57	(+0.83) +2.49	(+0.78) +1.88	(-0.89) -0.49
$\sigma_{eq} - \sigma_{ex}$ ($^\circ\text{C}$)	4.56	4.31	2.82	5.13
$\sigma_{eq} - \sigma_{ex,sum}$ ($^\circ\text{C}$)	(+1.50) +1.04	(+1.57) -1.03	(+0.92) -0.81	(+2.65) +2.03
$ \sigma_{glob} $ ($^\circ\text{C}$)	5.19	3.34	2.84	4.19
$ \sigma_{sum} $ ($^\circ\text{C}$)	(3.35) 3.64	(2.00) 3.33	(1.82) 2.83	(2.70) 3.06
Average ($^\circ\text{C}$)	4.03	2.75	2.01	3.31

Table 4. Model skill scores following a procedure comparable to the one presented by Lunt et al. (2012), for the model results of GH14, H18 and those presented here using the 42–38Ma SST proxy compilation from Figure 6 (see also Table S2). The last column considers the 38Ma $2\times\text{PIC}$ case and 38–34 Ma SST proxies (see Figure S9 and Table S3). Different measures are used (top to bottom); global, equatorial ($<23.5^\circ\text{N/S}$), extra-tropical ($>23.5^\circ\text{N/S}$), summer temperatures (only for $>23.5^\circ\text{N/S}$), meridional temperature gradient (i.e. equatorial - extra-tropical; annual or summer), global absolute and summer absolute error. Bracketed values indicate model skill using modelled summer temperatures only when they improve agreement with the corresponding proxy estimate. An average skill score for each model-proxy comparison is also determined by taking the root mean square of all the above measures and highlighted in bold.

An overview of model skill scores is given in Table 4, comparing modelled SSTs from the 45Ma $4\times\text{CO}_2$, 38Ma 800ppm ($2\times\text{CO}_2$) and $4\times\text{PIC}$ cases to 42–38 Ma proxies and those of the 38Ma $2\times\text{PIC}$ to 38–34 Ma proxies. Although all of the considered model cases simulate on average cooler SSTs than those suggested by the proxies ($\sigma_{glob} < 0$), a considerable improvement is seen for the new 38Ma cases (including H18). The equator-to-pole temperature gradient is still being overestimated by the models, but the discrepancy ($\sigma_{eq} - \sigma_{ex}$) is smallest for the 38Ma $4\times\text{PIC}$ case presented

600



here. As expected, better model skill is seen when considering summertime temperatures if they are highly underestimated by the annual mean. This is thus not the case for the 38Ma 4× PIC (and H18 800ppm CO₂) results, as the improvement at some sites is compensated by others for which the proxies are likely better estimates of annual mean SST (see also Figures 6 and 7). Those two model cases even underestimate the meridional gradient with summertime temperatures at extra-tropical locations, indicating that we cannot simply assume an overall summer-bias in those proxies or cold bias in the models. Indeed, a further improvement of the model-proxy agreement is seen when considering modelled summer temperatures only at those sites where they provide a better match with to the corresponding proxy estimate. For nearly all of the respective skill measures the 38Ma 4× PIC results show the best agreement with available 42–38 Ma SST proxies, followed closely by those of H18 using 800ppm CO₂.



3.4 Climate sensitivity

615 The global mean equilibrium temperature difference between our 38Ma 4× PIC and 2× PIC sim-
ulations (3.21°C; see Table 3) is similar to the model’s response to a CO₂ doubling in the pre-
industrial reference (3.14°C). Yet, the estimated radiative forcing from a second PIC doubling
($\Delta RF_{2\times}^{4\times} = 5.15\text{W/m}^2$) results in a considerably lower equilibrium climate sensitivity for our Eocene
simulations: $S_{EO} = 0.62^\circ\text{C/Wm}^{-2}$.

620 Even in this virtually ice-free world significant polar amplification is found, as the response to a PIC
doubling ranges between 2°C warming in low latitude regions to as much as 8°C at high latitudes
(~0.4–1.6 °C/Wm⁻²; see Figure 9a-b). Zonal variation in the warming signal is highest at middle
latitudes because of land-ocean contrasts, while differences in seasonal response are largest in polar
625 regions. The polar amplification signal is reflected by the differences in outgoing longwave radia-
tion, being increasingly positive towards higher latitudes (Planck feedback; Figure 9c-d). Overall
net negative longwave fluxes over equatorial regions can be explained by tropopause responses and
stratospheric cooling, which reduce outgoing radiation. On a more regional scale, alternating signals
of differences in shortwave and longwave radiation occur with a pronounced minimum at the equator
and maxima over the ITCZ locations. This suggests the importance of cloud cover, which is seen to
630 differ substantially (Figure 9e-f). An increase in deep convective clouds over the equatorial Pacific
corresponds to lower fluxes (more reflection of incoming shortwave and less outgoing longwave),
while the opposite is seen off the equator. Differences in cloud cover are seen to have a warming
effect over most of the high latitude regions. Increased wintertime low cloud cover over Antarctica
and reduced summertime low cloud cover over the Arctic, along with increased high cloud cover all
635 tend to warm the surface. The overall slight net heat loss (shortwave < longwave difference) at low
latitudes versus a gain at middle-high latitudes agrees with a reduced meridional heat flux seen in
the warmer 4× PIC climate (Figure 5).

As in the present-day climate the polar amplification is in part due to albedo effects from clouds, veg-
etation, snow cover and some seasonal sea ice, but also the result of a strong water vapour feedback
640 and meridionally dependent lapse rate feedback (less negative towards higher latitudes). Low latitude
regions, on the other hand, warm less as they are strongly governed by moist processes (i.e. cloud
cover and negative lapse rate feedback) and more tied to SSTs (low land fraction). An overview of
zonally averaged atmospheric temperature changes between some of the different model cases con-
sidered here can be found in Figure S14.

645

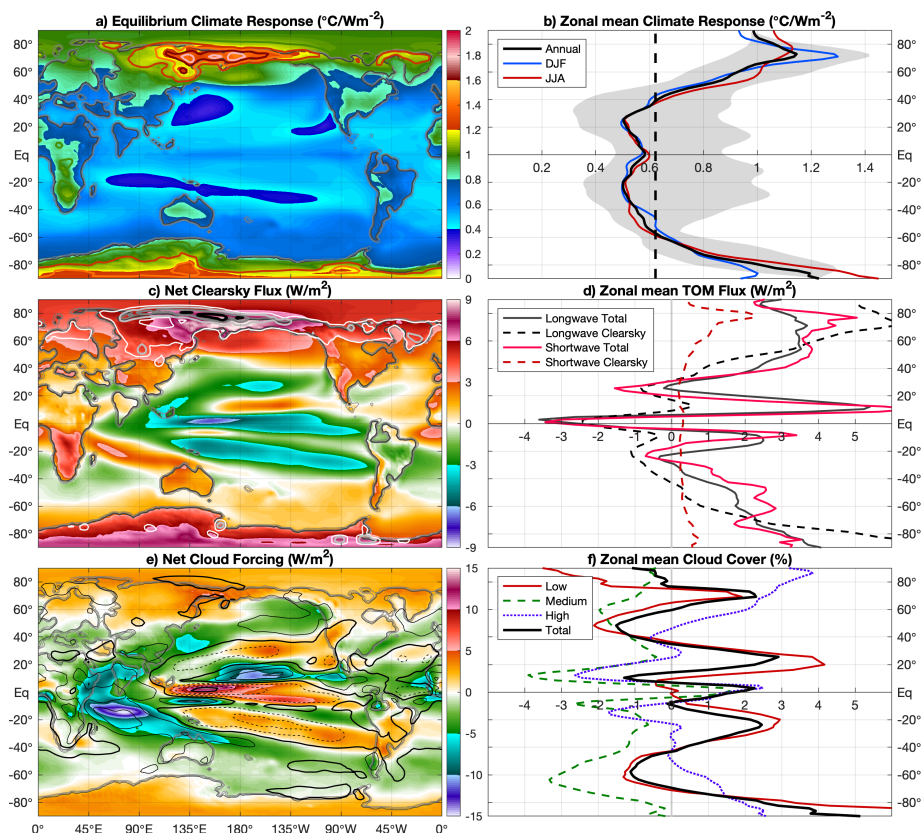


Figure 9. a) Annual mean temperature response, normalised per W/m^2 of the 38Ma $4\times$ PIC compared to the $2\times$ PIC equilibrium climate with contours showing the winter season only (using the same colour scale). b) Zonal mean normalised temperature response; annual (black), December-January-February (blue) and June-July-August (red). The grey shading indicates minimum and maximum values for each latitude of the annual mean. The (area-weighted) global average response (i.e. climate sensitivity) is $0.62^\circ\text{C/Wm}^{-2}$ and is indicated by the black dashed line. c) Clear-sky component of the net longwave flux change at the top of model (TOM) for $4\times$ PIC vs. $2\times$ PIC, similar for the clear-sky shortwave flux in contours (white to black; 1, 2, 5 and 10 W/m^2). d) Zonal mean TOM flux change for longwave (black) and shortwave (red) fluxes, corresponding clear-sky components are shown using dashed lines. Note that longwave fluxes are defined positive upward while shortwave fluxes are positive downward. e) Change in the total cloud forcing: longwave component (shading) and shortwave (contours every 5W/m^2 ; solid positive and dashed negative, thick black line at 0W/m^2). f) Zonal mean changes in cloud cover (in %) at low (solid red), medium (dashed green), high (dotted purple) and all (thick solid black) levels.



A list of averaged differences in our 38Ma 4× PIC and 2× PIC simulations with respect to the pre-industrial reference is presented in Table 5, considering global near surface air temperature (MAT_{glob}), equatorial SST (SST_{eq}) and deep ocean temperature (T_{deep}). Using equation 2, we can determine both the climate sensitivity S and integral geography effect G for the different
 650 measures. Not surprisingly, using MAT_{glob} yields the same value of $S_{EO} = 0.62^\circ\text{C/Wm}^{-2}$, with $G = 11.07\text{W/m}^2$ (so $G \sim 6.89^\circ\text{C}$). The estimate of G decreases when using only oceanic temperatures as the direct effect of cooler temperatures over pre-industrial land ice is removed. While considering global MAT differences will likely overestimate the effect of global geography changes (mainly through lapse-rate effects on ice sheets and mountains), the opposite is true for equatorial
 655 SSTs. The according results for S_{EO} show less variation between different methods as they are tied to the respective temperature changes between the 38Ma 2× PIC and 4× PIC cases. A possible range of $G = 6.08\text{--}11.10\text{ W/m}^2$ is found, equivalent to $\sim 1.6\text{--}2.6\text{ CO}_2$ doublings or a $4.2\text{--}6.9^\circ\text{C}$ warming globally.

Method	$\Delta T^{4\times}$ ($^\circ\text{C}$)	$\Delta T^{2\times}$ ($^\circ\text{C}$)	S_{EO} ($^\circ\text{C/Wm}^{-2}$)	G (W/m^2)
MAT_{glob}	12.71	9.514	0.622	11.10
SST_{eq}	10.64	7.08	0.690	6.08
T_{deep}	10.79	7.90	0.561	9.91

Table 5. Temperature differences comparing the 38Ma 4× PIC ($\Delta T^{4\times}$) and 2× PIC ($\Delta T^{2\times}$) Eocene climate to the pre-industrial reference, derived values for equilibrium climate sensitivity (S) and forcing from (integral) geography changes (G) using equation 2. Results are shown using global mean 2m temperature, equatorial SST (with a 3/2 ratio, as discussed in Royer et al. 2012) and deep sea temperature (below 2km).

A more direct estimate of G can be obtained by comparing a pre-industrial climate under 2× PIC
 660 and 4× PIC, with the results from the modelled 38Ma 2× PIC case. Using the model’s pre-industrial ECS ($S_{PI} = 0.79^\circ\text{C/Wm}^{-2}$) and radiative forcing of two consecutive PIC doublings ($\Delta\text{RF}^{2\times}$ and $\Delta\text{RF}^{4\times}$) yields an expected warming of 3.31°C and 7.39°C , respectively. As the modelled change in global mean temperature with respect to the pre-industrial reference is either 9.50°C (2× PIC) or 12.71°C (4× PIC), an additional warming of $5.32\text{--}6.19^\circ\text{C}$ takes place owing to integrated global
 665 geography changes (of which the effect is thus not entirely independent of the climatic state).

A similar exercise can be done for all of the different cases shown in Figure 10, using on one hand S_{EO} and on the other hand S_{PI} in combination with the previously defined values of RF and the available model results. The projected temperatures suggest a contribution of $\sim 10\%$ at 2× CO_2/PIC and $\sim 20\%$ at 4× CO_2/PIC from slow feedbacks (e.g. deep ocean, water vapour) to the global mean
 670 warming response. The respective equilibrium temperatures for either pre-industrial or Eocene climates then yield a consistent estimate of $G = 8.7\text{W/m}^2$, corresponding to a $5.3\text{--}6.9^\circ\text{C}$ global mean temperature difference.

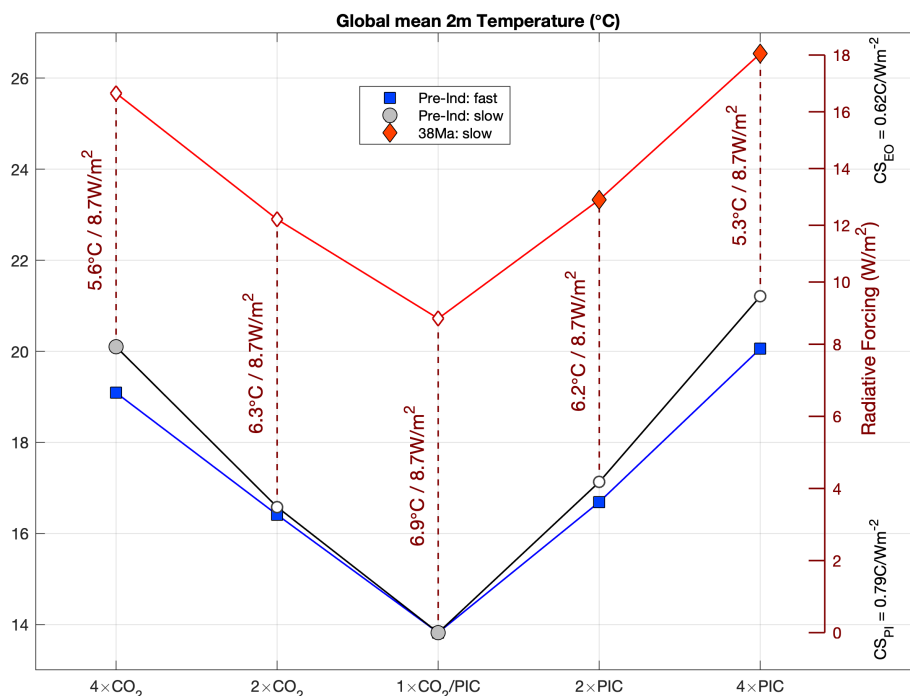


Figure 10. Overview of globally averaged near surface air temperatures in the different pre-industrial reference (blue) and 38Ma Eocene (red) simulations. Blue squares show the extrapolated temperature response of fast feedbacks from 20-year perturbations ($4\times\text{CO}_2$, $2\times\text{CO}_2$, $2\times\text{PIC}$ and $4\times\text{PIC}$, respectively), while grey circles also include that of slow feedbacks. Filled markers indicate results from equilibrated simulations, open markers show values that were estimated from the model-derived climate sensitivity and radiative forcing (red axis to the right; note the change in scale between pre-industrial and Eocene using S_{PI} and S_{EO} , respectively). Offsets in both temperature and radiative forcing (i.e. G) between pre-industrial and 38Ma Eocene cases are specified for all of the considered atmospheric compositions.

The possible range of G obtained here ($\sim 6\text{--}11\text{ W/m}^2$; $4\text{--}7^\circ\text{C}$) is considerably higher than either the estimated 1.8°C warming related to geography (using HadCM3L) found by Lunt et al. (2012) or the $\sim 2\text{--}4\text{ W/m}^2$ (i.e. $0.6\text{--}1.1\text{ CO}_2$ doublings) suggested by Royer et al. (2012). A comparably high warming of $\sim 5^\circ\text{C}$ from integral geography effects in the Eocene was proposed by Caballero and Huber (2013) and was found more recently for the early Eocene by Zhu et al. (2019). Higher estimates of $2\text{--}6^\circ\text{C}$ can also be deduced using the different models considered by Lunt et al. (2012).



4 Summary and conclusions

680 Using version 1.0.5 of the Community Earth System Model (CESM), we presented results of sim-
ulated 38Ma Eocene climates under both high ($4\times$ PIC) and moderate ($2\times$ PIC) concentrations of
 CO_2 and CH_4 , using the most recent palaeogeographic constraints. These are among the first sim-
ulations with a fully-coupled and detailed (CMIP5-like) climate model to study the middle-to-late
Eocene climate, using a new 38Ma geography reconstruction.

685

The 38Ma $4\times$ PIC case shows a warm climate with a global mean near surface air temperature
of 26.5°C (pre-industrial: 13.8°C) and a low equator-to-pole temperature gradient. The global heat
budget is approximately meridionally symmetric, which is reflected by the zonal mean temperature
pattern. Deep water formation occurs in the South Pacific Ocean, while the North Atlantic is sta-
bly stratified and stagnant due to the outflow of brackish Arctic waters. A shallow and rather weak
precursor of an Antarctic Circumpolar Current is found at a more southerly latitude than its present
equivalent, mainly driven by seasonally dependent wind stresses. Continental low/middle latitude
regions are characterised by high seasonality on both hemispheres and strong summer monsoons.
Middle and high latitudes mostly see mild winters, warm summers and pronounced storm tracks.

695 The Arctic is rather cool due to its geographic isolation and the Antarctic continental interior shows
strong seasonality with especially hot summers.

Comparing the 38Ma $4\times$ PIC simulation to the available 42–38 Ma sea surface and terrestrial tem-
perature proxy records, shows an overall good match at middle-to-high latitudes without low lati-
tudes being too hot. This indicates that the CESM is able to simulate the warm greenhouse climate
of the late middle Eocene (\sim Bartonian) without the need for extremely high ($>1200\text{ppm CO}_2$) at-
mospheric carbon. In the $2\times$ PIC simulation, the patterns of oceanic and atmospheric equilibrium
circulation are qualitatively very similar to those of the $4\times$ PIC one. Based on a similar compari-
son between model results and 38–34 Ma proxy temperature estimates, our 38Ma $2\times$ PIC case is a
good analog for the late Eocene climate (\sim Priabonian). While the model results are able to explain
Southern Ocean heterogeneity as well as Southwest Pacific warmth suggested by proxy records,
they disagree with indications of predominant westward flow through the Tasmanian Gateway dur-
ing most of the Eocene.

710 Previous Eocene simulations (at $4\times$ pre-industrial CO_2) with a similar model but a different (45Ma)
continental geography and lower resolution have resulted in overall similar sea surface temperature
distributions (Goldner et al., 2014). However, the 38Ma $4\times$ PIC case presented here is about $4\text{--}5^\circ\text{C}$
warmer globally in both SSTs and land temperatures. Comparable results were found by Hutchin-
son et al. (2018) for the late Eocene, using the same 38Ma geography reconstruction and the GFDL
715 CM2.1. Higher resolution and a more time-specific geography reconstruction allows for a better rep-



resentation of regional features, including equatorial upwelling, zonal heterogeneity in the Southern Ocean and Antarctic summer warmth. Higher temperatures in our simulations are the combined result a quadrupling of methane (radiative forcing $\sim 4.85 \times$ pre-industrial CO_2), different atmospheric grids (finite volume versus spectral), cloud parameterisations and higher spatial resolution in combination with a different geography reconstruction.

An equilibrium climate sensitivity of $S_{EO} = 0.62^\circ\text{C}/\text{Wm}^{-2}$ was found from the 38Ma $2 \times$ PIC and $4 \times$ PIC cases, which is lower than the same model's pre-industrial value ($S_{PI} = 0.79^\circ\text{C}/\text{Wm}^{-2}$). While some of the altered model boundary conditions for the Eocene cases add to increased temperatures with respect to the pre-industrial reference, they also act to reduce climate sensitivity (e.g. land-sea distribution and cloud cover). Water vapour and lapse rate feedbacks play crucial roles in both the reference state and sensitivity of the Eocene greenhouse climate. The model-derived radiative forcing from a second PIC doubling ($5.15\text{W}/\text{m}^2$) is much higher than that of a CO_2 doubling ($3.49\text{W}/\text{m}^2$). Even after 4600 model years the 38Ma $4 \times$ PIC simulation is still warming slightly, which adds to a possible underestimation of S_{EO} .

When also taking the pre-industrial reference into consideration, a fixed forcing $G \approx 9\text{W}/\text{m}^2$ from (integral) geography changes was estimated, corresponding to $\sim 6^\circ\text{C}$. Previous studies have noted this effect in terms of an offset in global mean temperature between pre-industrial and palaeoclimate simulations (Lunt et al., 2012; Farnsworth et al., 2019). Similar to what was found by Caballero and Huber (2013) the direct effect of ice sheet coverage is limited, leaving a considerable warming due to other geography-related changes. When using oceanic instead of atmospheric temperatures, the influence of topography and land surface changes is indeed reduced mostly by excluding the direct effect of the ice sheets and vegetation changes. Although smaller, the estimate of G from oceanic temperatures is still larger ($\sim 6\text{W}/\text{m}^2$; 4°C) than suggested in most previous studies. This indicates a major contribution to G from changes in continental geometry and the related circulation patterns, which our 38Ma simulations are better able to resolve.

Several peculiar (extreme) phenomena were found in the 38Ma CESM simulations. Extremely high ($\sim 50^\circ\text{C}$) summer temperatures occur in the sub-tropics under $4 \times$ PIC and are possibly related to fixed vegetation types, but cannot be disproven by the available proxies. Strong seasonality is seen on Antarctica, where summer temperatures reach up to 35°C in the $4 \times$ PIC case. The absence of an ice sheet, warm waters surrounding the continent and summertime insolation cause the Antarctic continent to become a heat island. Sea ice coverage is limited and only occurs sporadically during the winter months for the 38Ma $2 \times$ PIC case. Significant polar amplification is seen for a doubling of CO_2 and CH_4 , mainly due to changes in cloud cover and lapse rate feedbacks which tend to further reduce the meridional temperature gradient.



As the simulated middle-to-late Eocene (38Ma $2\times$ PIC and $4\times$ PIC) climate is in good agreement
755 with estimates from proxy records, the results presented here may be used to interpret proxy records
in more detail using the modelled circulation patterns.

Acknowledgements This work was carried out under the program of the Netherlands Earth Sys-
tem Science Centre (NESSC), financially supported by the Dutch Ministry of Education, Culture
760 and Science. The computations using CESM1.0.5 were done on the Cartesius at SURFsara in Am-
sterdam. The use of the SURFsara computing facilities was sponsored by NWO-EW (Netherlands
Organisation for Scientific Research, Exact Sciences) under the project 15508. The authors would
like to thank Dr. Nicholas Herold for his extensive help setting up the CESM and assisting to fix
numerous bugs and difficulties emerging with deep time palaeoclimate simulations. AvdH acknowl-
765 edges travel support to network partners from the EPSRC-funded Past Earth Network (Grant number
EP/M008363/1) and AS thanks the European Research Council for Consolidator Grant #771497.



References

- Abbot, D. S., Huber, M., Bousquet, G., and Walker, C. C.: High-CO₂ cloud radiative forcing feed-
770 back over both land and ocean in a global climate model, *Geophysical Research Letters*, 36, 2–5,
doi:10.1029/2008GL036703, 2009.
- Anagnostou, E., John, E. H., Edgar, K. M., Foster, G. L., Ridgwell, A., Inglis, G. N., Pancost, R. D., Lunt, D. J.,
and Pearson, P. N.: Changing atmospheric CO₂ concentration was the primary driver of early Cenozoic
climate, *Nature*, 533, 380–384, doi:10.1038/nature17423, <http://dx.doi.org/10.1038/nature17423>, 2016.
- 775 Baatsen, M. L. J., Van Hinsbergen, D. J. J., Von Der Heydt, A. S., Dijkstra, H. A., Sluijs, A., Abels, H. A.,
and Bijl, P. K.: Reconstructing geographical boundary conditions for palaeoclimate modelling during the
Cenozoic, *Climate of the Past*, 12, 1635–1644, doi:10.5194/cp-12-1635-2016, 2016.
- Beerling, D., Berner, R. A., Mackenzie, F. T., Harfoot, M. B., and Pyle, J. A.: Methane and the CH₄-
related greenhouse effect over the past 400 million years, *American Journal of Science*, 309, 97–113,
780 doi:10.2475/02.2009.01, 2009.
- Beerling, D. J. and Royer, D. L.: Convergent Cenozoic CO₂ history, *Nature Geoscience*, 4, 418–420,
doi:10.1038/ngeo1186, <http://www.nature.com/doi/10.1038/ngeo1186>, 2011.
- Beerling, D. J., Fox, A., Stevenson, D. S., and Valdes, P. J.: Enhanced chemistry-climate feedbacks
in past greenhouse worlds, *Proceedings of the National Academy of Sciences*, 108, 9770–9775,
785 doi:10.1073/pnas.1102409108, www.pnas.org/cgi/doi/10.1073/pnas.1102409108, 2011.
- Bellucci, A., Gualdi, S., and Navarra, A.: The double-ITCZ syndrome in coupled general circula-
tion models: The role of large-scale vertical circulation regimes, *Journal of Climate*, 23, 1127–1145,
doi:10.1175/2009JCLI3002.1, 2010.
- Bijl, P., Houben, A., Schouten, S., Bohaty, S., Sluijs, A., Reichert, G., Sinninghe Damsté, J., and Brinkhuis,
790 H.: Transient Middle Eocene atmospheric CO₂ and temperature variations., *Science*, 330, 819–821,
doi:10.1126/science.1193654, <http://www.ncbi.nlm.nih.gov/pubmed/21051636>, 2010.
- Bijl, P. K., Schouten, S., Sluijs, A., Reichert, G.-J., Zachos, J. C., and Brinkhuis, H.: Early Palaeogene
temperature evolution of the southwest Pacific Ocean., *Nature*, 461, 776–779, doi:10.1038/nature08399,
<http://dx.doi.org/10.1038/nature08399>, 2009.
- 795 Bijl, P. K., Bendle, J. A. P., Bohaty, S. M., Pross, J., Schouten, S., Tauxe, L., Stickley, C. E., McKay,
R. M., Röhl, U., Olney, M., Sluijs, A., Escutia, C., and Brinkhuis, H.: Eocene cooling linked to early flow
across the Tasmanian Gateway., *Proceedings of the National Academy of Sciences of the United States
of America*, 110, 9645–9650, doi:10.1073/pnas.1220872110, [http://www.pnas.org/content/early/2013/05/28/
1220872110.abstract](http://www.pnas.org/content/early/2013/05/28/1220872110.abstract), 2013.
- 800 Bitz, C. M., Shell, K. M., Gent, P. R., Bailey, D. A., Danabasoglu, G., Armour, K. C., Holland, M. M., and
Kiehl, J. T.: Climate sensitivity of the community climate system model, version 4, *Journal of Climate*, 25,
3053–3070, doi:10.1175/JCLI-D-11-00290.1, 2012.
- Blackmon, M., Boville, B., Bryan, F., Dickinson, R., Gent, P., Kiehl, J., Moritz, R., Randall, D., Shukla, J.,
Solomon, S., Bonan, G., Doney, S., Fung, I., Hack, J., Hunke, E., Hurrell, J., Kutzbach, J., Meehl, J., Otto-
805 bliessner, B., Saravanan, R., Schneider, E. K., Sloan, L., Spall, M., Taylor, K., Tribbia, J., and Washington, W.:
The Community Climate System Model, *Bulletin of the American Meteorological Society*, 82, 2357–2376,
doi:10.1175/1520-0477(2001)082<2357:TCCSM>2.3.CO;2, 2001.



- Bohaty, S. M. and Zachos, J. C.: Significant Southern Ocean warming event in the late middle Eocene, *Geology*, 31, 1017–1020, doi:10.1130/G19800.1, 2003.
- 810 Bosboom, R. E., Abels, H. A., Hoorn, C., van den Berg, B. C. J., Guo, Z., and Dupont-Nivet, G.: Aridification in continental Asia after the Middle Eocene Climatic Optimum (MECO), *Earth and Planetary Science Letters*, 389, 34–42, doi:10.1016/j.epsl.2013.12.014, <http://dx.doi.org/10.1016/j.epsl.2013.12.014>, 2014.
- Boyle, B., Meyer, H., Enquist, B., and Salas, S.: Higher taxa as paleoecological and paleoclimatic indicators: A search for the modern analog of the Florissant fossil flora, in: *Paleontology of the Upper Eocene Florissant Formation, Colorado*, edited by Meyer, H. W. and Smith, D. M., chap. 3, pp. 33–51, The Geological Society of America, 2008.
- 815 Caballero, R. and Huber, M.: State-dependent climate sensitivity in past warm climates and its implications for future climate projections, *Proceedings of the National Academy of Sciences*, 110, 14 162–14 167, doi:10.1073/pnas.1303365110, <http://www.pnas.org/cgi/doi/10.1073/pnas.1303365110>, 2013.
- 820 Carter, A., Riley, T. R., Hillenbrand, C. D., and Rittner, M.: Widespread Antarctic glaciation during the Late Eocene, *Earth and Planetary Science Letters*, 458, 49–57, doi:10.1016/j.epsl.2016.10.045, <http://dx.doi.org/10.1016/j.epsl.2016.10.045>, 2017.
- Conte, M. H., Sicre, M. A., Rühlemann, C., Weber, J. C., Schulte, S., Schulz-Bull, D., and Blanz, T.: Global temperature calibration of the alkenone unsaturation index (U37k) in surface waters and comparison with surface sediments, *Geochemistry, Geophysics, Geosystems*, 7, doi:10.1029/2005GC001054, 2006.
- 825 Coxall, H. K., Wilson, P. a., Pälike, H., Lear, C. H., and Backman, J.: Rapid stepwise onset of Antarctic glaciation and deeper calcite compensation in the Pacific Ocean., *Nature*, 433, 53–57, doi:10.1038/nature03135, 2005.
- Coxall, H. K., Huck, C. E., Huber, M., Lear, C. H., Legarda-Lisarri, A., O'Regan, M., Sliwinska, K. K., van de Flierdt, T., de Boer, A. M., Zachos, J. C., and Backman, J.: Export of nutrient rich Northern Component Water preceded early Oligocene Antarctic glaciation, *Nature Geoscience*, 11, 190–196, doi:10.1038/s41561-018-0069-9, <http://www.nature.com/articles/s41561-018-0069-9>, 2018.
- 830 Cramer, B. S., Toggweiler, J. R., Wright, J. D., Katz, M. E., and Miller, K. G.: Ocean overturning since the late cretaceous: Inferences from a new benthic foraminiferal isotope compilation, *Paleoceanography*, 24, 1–14, doi:10.1029/2008PA001683, 2009.
- 835 Cramwinckel, M. J., Huber, M., Kocken, I. J., Agnini, C., Bijl, P. K., Bohaty, S. M., Frieling, J., Goldner, A., Hilgen, F. J., Kip, E. L., Peterse, F., Van Der Ploeg, R., Röhl, U., Schouten, S., and Sluijs, A.: Synchronous tropical and polar temperature evolution in the Eocene letter, *Nature*, 559, 382–386, doi:10.1038/s41586-018-0272-2, 2018.
- 840 Cramwinckel, M. J., Woelders, L., Huurdeman, E. P., Peterse, F., Stephen, J., Pross, J., Burgess, C. E., Reichart, G.-j., Sluijs, A., and Bijl, P. K.: Surface-circulation change in the Southern Ocean across the Middle Eocene Climatic Optimum : inferences from dinoflagellate cysts and biomarker paleothermometry, 2019.
- Danabasoglu, G., Ferrari, R., and McWilliams, J. C.: Sensitivity of an ocean general circulation model to a parameterization of near-surface eddy fluxes, *Journal of Climate*, 21, 1192–1208, doi:10.1175/2007JCLI1508.1, 2008.
- 845



- Danabasoglu, G., Bates, S. C., Briegleb, B. P., Jayne, S. R., Jochum, M., Large, W. G., Peacock, S., and Yeager, S. G.: The CCSM4 ocean component, *Journal of Climate*, 25, 1361–1389, doi:10.1175/JCLI-D-11-00091.1, 2012.
- DeConto, R. M. and Pollard, D.: Rapid Cenozoic glaciation of Antarctica induced by declining atmospheric
850 CO₂, *Nature*, 421, 245–249, doi:10.1038/nature01290, 2003.
- DeConto, R. M., Pollard, D., Wilson, P. a., Pälike, H., Lear, C. H., and Pagani, M.: Thresholds for Cenozoic bipolar glaciation., *Nature*, 455, 652–656, doi:10.1038/nature07337, 2008.
- Douglas, P. M. J., Affek, H. P., Ivany, L. C., Houben, A. J. P., Sijp, W. P., Sluijs, A., Schouten, S., and Pagani, M.: Pronounced zonal heterogeneity in Eocene southern high-latitude sea surface temperatures, *Proceedings of the National Academy of Sciences*, 111, 6582–6587, doi:10.1073/pnas.1321441111, <http://www.pnas.org/cgi/doi/10.1073/pnas.1321441111>, 2014.
855
- Eldrett, J. S., Greenwood, D. R., Harding, I. C., and Huber, M.: Increased seasonality through the Eocene to Oligocene transition in northern high latitudes, *Nature*, 459, 969–973, doi:10.1038/nature08069, 2009.
- England, M. H.: the Age of Water and Ventilation Timescales in a Global Ocean Model, doi:10.1175/1520-
860 0485(1995)0252.0.CO;2, 1995.
- Etminan, M., Myhre, G., Highwood, E. J., and Shine, K. P.: Radiative forcing of carbon dioxide, methane, and nitrous oxide: A significant revision of the methane radiative forcing, *Geophysical Research Letters*, 43, 12,614–12,623, doi:10.1002/2016GL071930, 2016.
- Evans, D., Sagoo, N., Renema, W., Cotton, L. J., Müller, W., Todd, J. A., Saraswati, P. K., Stassen, P., Ziegler, M., Pearson, P. N., Valdes, P. J., and Affek, H. P.: Eocene greenhouse climate revealed by coupled clumped isotope-Mg/Ca thermometry., *Proceedings of the National Academy of Sciences of the United States of America*, p. 201714744, doi:10.1073/pnas.1714744115, <http://www.ncbi.nlm.nih.gov/pubmed/29358374>, 2018.
865
- Farnsworth, A., Lunt, D. J., Brien, C. L. O., and Foster, G. L.: Climate Sensitivity on Geological Timescales Controlled by Nonlinear Feedbacks and Ocean Circulation, 2019.
870
- Gasson, E., Lunt, D. J., Deconto, R., Goldner, A., Heinemann, M., Huber, M., Legrande, a. N., Pollard, D., Sagoo, N., Siddall, M., Winguth, A., and Valdes, P. J.: Uncertainties in the modelled CO₂ threshold for Antarctic glaciation, *Climate of the Past*, 10, 451–466, doi:10.5194/cp-10-451-2014, 2014.
- Gent, P. R. and McWilliams, J. C.: Isopycnal Mixing in Ocean Circulation Models, doi:10.1175/1520-
875 0485(1990)020<0150:IMIOCM>2.0.CO;2, 1990.
- Gent, P. R., Danabasoglu, G., Donner, L. J., Holland, M. M., Hunke, E. C., Jayne, S. R., Lawrence, D. M., Neale, R. B., Rasch, P. J., Vertenstein, M., Worley, P. H., Yang, Z. L., and Zhang, M.: The community climate system model version 4, *Journal of Climate*, 24, 4973–4991, doi:10.1175/2011JCLI4083.1, 2011.
- Goldner, A., Herold, N., and Huber, M.: Antarctic glaciation caused ocean circulation changes at the
880 Eocene–Oligocene transition, *Nature*, 511, 574–577, doi:10.1038/nature13597, <https://www.nature.com/articles/nature13597>, 2014.
- Greenwood, D. R. and Wing, S. L.: Eocene continental climates and latitudinal temperature gradients, *Geology*, 23, 1044–1048, doi:10.1130/0091-7613(1995)023<1044:ECCALT>2.3.CO;2, 1995.



- Greenwood, D. R., Wilf, P., Wing, S. L., and Christophel, D. C.: Paleotemperature Estimation
885 Using Leaf-Margin Analysis: Is Australia Different?, *PALAIOS*, 19, 129–142, doi:10.1669/0883-1351(2004)019<0129:PEULAI>2.0.CO;2, 2004.
- Gregory, J. M., Ingram, W. J., Palmer, M. A., Jones, G. S., Stott, P. A., Thorpe, R. B., Lowe, J. A., Johns, T. C.,
and Williams, K. D.: A new method for diagnosing radiative forcing and climate sensitivity, *Geophysical
Research Letters*, 31, 2–5, doi:10.1029/2003GL018747, 2004.
- 890 Gregory-Wodzicki, K. M.: The Late Eocene House Range Flora, Sevier Desert, Utah: Paleoclimate and Paleoelevation, *PALAIOS*, 12, 552–567, doi:10.2307/3515411, 1997.
- Hague, A. M., Thomas, D. J., Huber, M., Korty, R., Woodard, S. C., and Jones, L. B.: Convection of North
Pacific deep water during the early Cenozoic, *Geology*, 40, 527–530, doi:10.1130/G32886.1, 2012.
- Heavens, N. G., Shields, C. A., and Mahowald, N. M.: A paleogeographic approach to aerosol prescrip-
895 tion in simulations of deep time climate, *Journal of Advances in Modeling Earth Systems*, 4, 1–13,
doi:10.1029/2012MS000166, 2012.
- Herold, N., Buzan, J., Seton, M., Goldner, A., Green, J. a. M., Müller, R. D., Markwick, P., and Huber, M.: A
suite of Early Eocene (~55 Ma) climate model boundary conditions, *Geoscientific Model Development*, 7,
2077–2090, doi:10.5194/gmd-7-2077-2014, www.geosci-model-dev.net/7/2077/2014/, 2014.
- 900 Hill, D. J., Haywood, A. M., Valdes, P. J., Francis, J. E., Lunt, D. J., Wade, B. S., and Bowman, V. C.: Paleogeographic controls on the onset of the Antarctic circumpolar current, *Geophysical Research Letters*, 40,
5199–5204, doi:10.1002/grl.50941, 2013.
- Hines, B. R., Hollis, C. J., Atkins, C. B., Baker, J. A., Morgans, H. E., and Strong, P. C.: Reduction of
oceanic temperature gradients in the early Eocene Southwest Pacific Ocean, *Palaeogeography, Palaeocli-
905 matology, Palaeoecology*, 475, 41–54, doi:10.1016/j.palaeo.2017.02.037, http://dx.doi.org/10.1016/j.palaeo.2017.02.037, 2017.
- Hinojosa, L. F. and Villagrán, C.: Did South American Mixed Paleofloras evolve under thermal equability or
in the absence of an effective Andean barrier during the Cenozoic?, *Palaeogeography, Palaeoclimatology,
Palaeoecology*, 217, 1–23, doi:10.1016/j.palaeo.2004.11.013, 2005.
- 910 Hollis, C. J., Taylor, K. W., Handley, L., Pancost, R. D., Huber, M., Creech, J. B., Hines, B. R., Crouch, E. M.,
Morgans, H. E., Crampton, J. S., Gibbs, S., Pearson, P. N., and Zachos, J. C.: Early Paleogene temperature
history of the Southwest Pacific Ocean: Reconciling proxies and models, *Earth and Planetary Science Letters*,
349–350, 53–66, doi:10.1016/j.epsl.2012.06.024, http://dx.doi.org/10.1016/j.epsl.2012.06.024, 2012.
- Hollis, C. J., Dunkley Jones, T., Anagnostou, E., Bijl, P. K., Cramwinckel, M. J., Cui, Y., Dickens, G. R., Edgar,
915 K. M., Eley, Y., Evans, D., Foster, G. L., Frieling, J., Inglis, G. N., Kennedy, E. M., Kozdon, R., Laurentano,
V., Lear, C. H., Littler, K., Lourens, L., Nele Meckler, A., Naafs, B. D. A., Pälike, H., Pancost, R. D., Pearson,
P. N., Röhl, U., Royer, D. L., Salzmann, U., Schubert, B. A., Seebeck, H., Sluijs, A., Speijer, R. P., Stassen,
P., Tierney, J., Tripathi, A., Wade, B., Westerhold, T., Witkowski, C., Zachos, J. C., Ge Zhang, Y., Huber, M.,
and Lunt, D. J.: The DeepMIP contribution to PMIP4: Methodologies for selection, compilation and analysis
920 of latest Paleocene and early Eocene climate proxy data, incorporating version 0.1 of the DeepMIP database,
Geoscientific Model Development, 12, 3149–3206, doi:10.5194/gmd-12-3149-2019, 2019.
- Hoskins, B. J. and Karoly, D. J.: The Steady Linear Response of a Spherical Atmosphere to Thermal and
Orographic Forcing, doi:10.1175/1520-0469(1981)038<1179:TSLROA>2.0.CO;2, 1981.



- Houben, A. J., Bijl, P. K., Sluijs, A., Schouten, S., and Brinkhuis, H.: Late Eocene Southern Ocean Cooling and
925 Invigoration of Circulation Preconditioned Antarctica for Full-Scale Glaciation, *Geochemistry, Geophysics, Geosystems*, 20, 2214–2234, doi:10.1029/2019GC008182, 2019.
- Huber, M. and Caballero, R.: The early Eocene equable climate problem revisited, *Climate of the Past*, 7, 603–
633, doi:10.5194/cp-7-603-2011, 2011.
- Huber, M. and Sloan, L. C.: Heat transport, deep waters, and thermal gradients: Coupled simulation of an
930 Eocene greenhouse climate, *Geophysical Research Letters*, 28, 3481–3484, doi:10.1029/2001GL012943,
<http://doi.wiley.com/10.1029/2001GL012943>, 2001.
- Huber, M., Brinkhuis, H., Stickley, C. E., Döös, K., Sluijs, A., Warnaar, J., Schellenberg, S. A., and Williams,
G. L.: Eocene circulation of the Southern Ocean: Was Antarctica kept warm by subtropical waters?, *Paleo-*
oceanography, 19, 1–12, doi:10.1029/2004PA001014, 2004.
- 935 Hunke, E. C. and Lipscomb, W. H.: The Los Alamos sea ice model, documentation and software., Tech. Rep.
LA-CC-06-012, version 4., 2008.
- Hurrell, J. W., Holland, M. M., Gent, P. R., Ghan, S., Kay, J. E., Kushner, P. J., Lamarque, J. F., Large, W. G.,
Lawrence, D., Lindsay, K., Lipscomb, W. H., Long, M. C., Mahowald, N., Marsh, D. R., Neale, R. B., Rasch,
P., Vavrus, S., Vertenstein, M., Bader, D., Collins, W. D., Hack, J. J., Kiehl, J., and Marshall, S.: The commu-
940 nity earth system model: A framework for collaborative research, *Bulletin of the American Meteorological*
Society, 94, 1339–1360, doi:10.1175/BAMS-D-12-00121.1, 2013.
- Hutchinson, D. K., de Boer, A. M., Coxall, H. K., Caballero, R., Nilsson, J., and Baatsen, M.: Climate sensitivity
and meridional overturning circulation in the late Eocene using GFDL CM2.1, *Climate of the Past*, 14, 789–
810, doi:10.5194/cp-14-789-2018, 2018.
- 945 Inglis, G. N., Farnsworth, A., Lunt, D. J., Foster, G. L., Hollis, C. J., Pagani, M., Jardine, P. E., Pearson, P. N.,
Markwick, P., and Galsworthy, A. M. J.: cooling inferred from GDGT distributions, *Paleoceanography*, 30,
1000–1020, doi:10.1002/2014PA002723, 2015.
- Kamp, P. J., Waghorn, D. B., and Nelson, C. S.: Late eocene-early oligocene integrated isotope stratigraphy
and biostratigraphy for paleoshelf sequences in southern Australia: paleoceanographic implications, *Palaeo-*
950 *geography, Palaeoclimatology, Palaeoecology*, 80, 311–323, doi:10.1016/0031-0182(90)90140-3, 1990.
- Kay, J. E., Holland, M. M., Bitz, C. M., Blanchard-Wrigglesworth, E., Gettelman, A., Conley, A., and Bailey,
D.: The influence of local feedbacks and northward heat transport on the equilibrium arctic climate response
to increased greenhouse gas forcing, *Journal of Climate*, 25, 5433–5450, doi:10.1175/JCLI-D-11-00622.1,
2012.
- 955 Kennedy, A. T., Farnsworth, A., Lunt, D. J., Lear, C. H., and Markwick, P. J.: Atmospheric and oceanic
impacts of Antarctic glaciation across the Eocene-Oligocene transition, *Philosophical Transactions of the*
Royal Society A: Mathematical, Physical and Engineering Sciences, 373, doi:10.1098/rsta.2014.0419,
<https://royalsocietypublishing.org/doi/full/10.1098/rsta.2014.0419>, 2015.
- Kiehl, J. T. and Shields, C. A.: Sensitivity of the Palaeocene-Eocene Thermal Maximum climate to cloud
960 properties, *Phil Trans R Soc A*, 371, 1–22, doi:10.1098/rsta.2013.0093, 2013.
- Kiehl, J. T., Shields, C. A., Hack, J. J., and Collins, W. D.: The climate sensitivity of the Community Climate
System Model version 3 (CCSM3), *Journal of Climate*, 19, 2584–2596, doi:10.1175/JCLI3747.1, [https://](https://journals.ametsoc.org/doi/full/10.1175/JCLI3747.1)
journals.ametsoc.org/doi/full/10.1175/JCLI3747.1, 2006.



- Kim, J. H., Schouten, S., Hopmans, E. C., Donner, B., and Sinninghe Damsté, J. S.: Global sediment core-top
965 calibration of the TEX86 paleothermometer in the ocean, *Geochimica et Cosmochimica Acta*, 72, 1154–
1173, doi:10.1016/j.gca.2007.12.010, 2008.
- Kim, J. H., van der Meer, J., Schouten, S., Helmke, P., Willmott, V., Sangiorgi, F., Koç, N., Hopmans, E. C., and
Damsté, J. S.: New indices and calibrations derived from the distribution of crenarchaeal isoprenoid tetraether
lipids: Implications for past sea surface temperature reconstructions, *Geochimica et Cosmochimica Acta*, 74,
970 4639–4654, doi:10.1016/j.gca.2010.05.027, 2010.
- Kobashi, T., Grossman, E. L., Dockery, D. T., and Ivany, L. C.: Water mass stability reconstructions from
greenhouse (Eocene) to icehouse (Oligocene) for the northern Gulf Coast continental shelf (USA), *Paleo-
oceanography*, 19, doi:10.1029/2003PA000934, <http://doi.wiley.com/10.1029/2003PA000934>, 2004.
- Kowalski, E. A. and Dilcher, D. L.: Warmer paleotemperatures for terrestrial ecosystems, *Proceedings of the
975 National Academy of Sciences*, 100, 167–170, doi:10.1073/pnas.232693599, <http://www.pnas.org/cgi/doi/10.1073/pnas.232693599>, 2003.
- Ladant, J.-B., Donnadiou, Y., Lefebvre, V., and Dumas, C.: The respective role of atmospheric carbon dioxide
and orbital parameters on ice sheet evolution at the Eocene-Oligocene transition, *Paleoceanography*, 29,
810–823, doi:10.1002/2013PA002593, 2014.
- 980 Large, W. G., McWilliams, J. C., and Doney, S. C.: Oceanic Vertical Mixing - a Review and a Model with a
Nonlocal Boundary-Layer Parameterization, *Reviews of Geophysics*, 32, 363–403, doi:10.1029/94rg01872,
1994.
- Lawrence, D. M., Oleson, K. W., Flanner, M. G., Thornton, P. E., Swenson, S. C., Lawrence, P. J., Zeng,
X., Yang, Z.-L., Levis, S., Sakaguchi, K., Bonan, G. B., and Slater, A. G.: Parameterization improvements
985 and functional and structural advances in Version 4 of the Community Land Model, *Journal of Advances in
Modeling Earth Systems*, 3, doi:10.1029/2011MS00045, <http://doi.wiley.com/10.1029/2011MS00045>, 2011.
- Lear, C. H., Bailey, T. R., Pearson, P. N., Coxall, H. K., and Rosenthal, Y.: Cooling and ice growth across the
Eocene-Oligocene transition, *Geology*, 36, 251–254, doi:10.1130/G24584A.1, 2008.
- Licht, a., van Cappelle, M., Abels, H. a., Ladant, J.-B., Trabucho-Alexandre, J., France-Lanord, C., Donnadiou,
990 Y., Vandenberghe, J., Rigaudier, T., Lécuyer, C., Terry, D., Adriaens, R., Boura, A., Guo, Z., Soe, A. N.,
Quade, J., Dupont-Nivet, G., and Jaeger, J.-J.: Asian monsoons in a late Eocene greenhouse world., *Nature*,
513, 501–506, doi:10.1038/nature13704, 2014.
- Liu, Z., Pagani, M., Zinniker, D., Deconto, R., Huber, M., Brinkhuis, H., Shah, S. R., Leckie, R. M., and
Pearson, A.: Global Cooling During the Eocene-Oligocene Climate Transition, *Science*, 323, 1187–1190,
995 2009.
- Loptson, C. A., Lunt, D. J., and Francis, J. E.: Investigating vegetation-climate feedbacks during the early
Eocene, *Climate of the Past*, 10, 419–436, doi:10.5194/cp-10-419-2014, 2014.
- Lunt, D. J., Jones, T. D., Heinemann, M., Huber, M., LeGrande, A., Winguth, A., Loptson, C., Marotzke, J.,
Roberts, C. D., Tindall, J., Valdes, P., and Winguth, C.: A model-data comparison for a multi-model ensemble
1000 of early Eocene atmosphere-ocean simulations: EoMIP, *Climate of the Past*, 8, 1717–1736, doi:10.5194/cp-
8-1717-2012, 2012.



- Lunt, D. J., Farnsworth, A., Loptson, C., L Foster, G., Markwick, P., O'Brien, C. L., Pancost, R. D., Robinson, S. A., and Wrobel, N.: Palaeogeographic controls on climate and proxy interpretation, *Climate of the Past*, 12, 1181–1198, doi:10.5194/cp-12-1181-2016, 2016.
- 1005 Neale, R. B., Richter, J., Park, S., Lauritzen, P. H., Vavrus, S. J., Rasch, P. J., and Zhang, M.: The Mean Climate of the Community Atmosphere Model (CAM4) in Forced SST and Fully Coupled Experiments, *Journal of Climate*, 26, 5150–5168, doi:10.1175/JCLI-D-12-00236.1, 2013.
- O'Brien, C. L., Robinson, S. A., Pancost, R. D., Sinninghe Damsté, J. S., Schouten, S., Lunt, D. J., Alsenz, H., Bornemann, A., Bottini, C., Brassell, S. C., Farnsworth, A., Forster, A., Huber, B. T., Inglis, G. N., Jenkyns, H. C., Linnert, C., Littler, K., Markwick, P., McAnena, A., Mutterlose, J., Naafs, B. D. A., Püttmann, W., Sluijs, A., van Helmond, N. A., Vellekoop, J., Wagner, T., and Wrobel, N. E.: Cretaceous sea-surface temperature evolution: Constraints from TEX86 and planktonic foraminiferal oxygen isotopes, *Earth-Science Reviews*, 172, 224–247, doi:10.1016/j.earscirev.2017.07.012, <https://doi.org/10.1016/j.earscirev.2017.07.012>, 2017.
- 1010
- 1015 Okafor, C. U., Thomas, D. J., Wade, B. S., and Firth, J.: Environmental change in the subtropics during the late middle Eocene greenhouse and global implications, *Geochemistry, Geophysics, Geosystems*, 10, 1–13, doi:10.1029/2009GC002450, 2009.
- Oleson, K. W., Lawrence, D. M., Gordon, B., Flanner, M. G., Kluzek, E., Peter, J., Levis, S., Swenson, S. C., Thornton, E., Dai, A., Decker, M., Dickinson, R., Feddema, J., Heald, C. L., Lamarque, J.-f., Liu, G.-y., Qian, T., Running, S., Sakaguchi, K., Slater, A., Stöckli, R., Wang, A., Yang, L., Zeng, X., and Zeng, X.: Technical Description of version 4.0 of the Community Land Model (CLM), NCAR Tech. Note, NCAR/TN-47, 2010.
- 1020
- Passchier, S., Bohaty, S. M., Jiménez-Espejo, F., Pross, J., Röhl, U., Van De Flierdt, T., Escutia, C., and Brinkhuis, H.: Early eocene to middle miocene cooling and aridification of east antarctica, *Geochemistry, Geophysics, Geosystems*, 14, 1399–1410, doi:10.1002/ggge.20106, 2013.
- 1025
- Passchier, S., Ciarletta, D. J., Miriagos, T. E., Bijl, P. K., and Bohaty, S. M.: An antarctic stratigraphic record of stepwise ice growth through the eocene-oligocene transition, *Bulletin of the Geological Society of America*, 129, 318–330, doi:10.1130/B31482.1, 2017.
- Pearson, P. N., Ditchfield, P. W., Singano, J., Harcourt-Brown, K. G., Nicholas, C. J., Olsson, R. K., Shackleton, N. J., and Hall, M. A.: Warm tropical sea surface temperatures in the Late Cretaceous and Eocene epochs, *Nature*, 413, 481–487, doi:10.1038/35097000, 2001.
- 1030
- Pearson, P. N., van Dongen, B. E., Nicholas, C. J., Pancost, R. D., Schouten, S., Singano, J. M., and Wade, B. S.: Stable warm tropical climate through the Eocene Epoch, *Geology*, 35, 211–214, doi:10.1130/G23175A.1, 2007.
- Peterse, F., van der Meer, J., Schouten, S., Weijers, J. W. H., Fierer, N., Jackson, R. B., Kim, J. H., and Sinninghe Damsté, J. S.: Revised calibration of the MBT-CBT paleotemperature proxy based on branched tetraether membrane lipids in surface soils, *Geochimica et Cosmochimica Acta*, 96, 215–229, doi:10.1016/j.gca.2012.08.011, 2012.
- 1035
- Petersen, S. V. and Schrag, D. P.: Antarctic ice growth before and after the Eocene-Oligocene transition: New estimates from clumped isotope paleothermometry, *Paleoceanography*, 30, 1305–1317, doi:10.1002/2014PA002769, 2015.
- 1040



- Prothero, D. R.: No Title, in: *Paleontology of the Upper Eocene Florissant Formation, Colorado*, edited by Meyer, H. W. and Smith, D. M., chap. 5, pp. 71–87, The Geological Society of America, Boulder, CO, 2008.
- Quan, C., Liu, Y. S. C., and Utescher, T.: Eocene monsoon prevalence over China: A paleobotanical perspective, *Palaeogeography, Palaeoclimatology, Palaeoecology*, 365–366, 302–311, doi:10.1016/j.palaeo.2012.09.035, 1045 <http://dx.doi.org/10.1016/j.palaeo.2012.09.035>, 2012.
- Retallack, G. J., Orr, W. N., Prothero, D. R., Duncan, R. A., Kester, P. R., and Ambers, C. P.: Eocene-Oligocene extinction and paleoclimatic change near Eugene, Oregon, *Bulletin of the Geological Society of America*, 116, 817–839, doi:10.1130/B25281.1, 2004.
- Royer, D. L., Pagani, M., and Beerling, D. J.: Geobiological constraints on Earth system sensitivity to CO₂ 1050 2 during the Cretaceous and Cenozoic, *Geobiology*, 10, 298–310, doi:10.1111/j.1472-4669.2012.00320.x, 2012.
- Scher, H. D., Bohaty, S. M., Smith, B. W., and Munn, G. H.: Eocene glaciation, *Paleoceanography*, 29, 628–644, doi:10.1002/2014PA002648, 2014.
- Schouten, S., Eldrett, J., Greenwood, D. R., Harding, I., Baas, M., and Damsté, J. S.: Onset of long-term cooling 1055 of Greenland near the Eocene-Oligocene boundary as revealed by branched tetraether lipids, *Geology*, 36, 147–150, doi:10.1130/G24332A.1, 2008.
- Schouten, S., Hopmans, E. C., and Sinninghe Damsté, J. S.: The organic geochemistry of glycerol dialkyl glycerol tetraether lipids: A review, *Organic Geochemistry*, 54, 19–61, doi:10.1016/j.orggeochem.2012.09.006, <http://dx.doi.org/10.1016/j.orggeochem.2012.09.006>, 2013.
- 1060 Sewall, J., Sloan, L., Huber, M., and Wing, S.: Climate sensitivity to changes in land surface characteristics, *Global and Planetary Change*, 26, 445–465, doi:10.1016/S0921-8181(00)00056-4, [https://doi.org/10.1016/S0921-8181\(00\)00056-4](https://doi.org/10.1016/S0921-8181(00)00056-4), 2000.
- Sijp, W. P., von der Heydt, A. S., Dijkstra, H. a., Flögel, S., Douglas, P. M. J., and Bijl, P. K.: The role of ocean gateways on cooling climate on long time scales, *Global and Planetary Change*, 119, 1–22, 1065 doi:10.1016/j.gloplacha.2014.04.004, <http://dx.doi.org/10.1016/j.gloplacha.2014.04.004>, 2014.
- Sijp, W. P., Von Der Heydt, A. S., and Bijl, P. K.: Model simulations of early westward flow across the Tasman Gateway during the early Eocene, *Climate of the Past*, 12, 807–817, doi:10.5194/cp-12-807-2016, 2016.
- 1070 Sluijs, A., Schouten, S., Pagani, M., Woltering, M., Brinkhuis, H., Damsté, J. S., Dickens, G. R., Huber, M., Reichart, G. J., Stein, R., Matthiessen, J., Lourens, L. J., Pedentchouk, N., Backman, J., Moran, K., Clemens, S., Cronin, T., Eynaud, F., Gattacceca, J., Jakobsson, M., Jordan, R., Kaminski, M., King, J., Koc, N., Martinez, N. C., McInroy, D., Moore, T. C., O'Regan, M., Onodera, J., Pälike, H., Rea, B., Rio, D., Sakamoto, T., Smith, D. C., St John, K. E., Suto, I., Suzuki, N., Takahashi, K., Watanabe, M., and Yamamoto, M.: Sub-tropical Arctic Ocean temperatures during the Palaeocene/Eocene thermal maximum, *Nature*, 441, 610–613, doi:10.1038/nature04668, 2006.
- 1075 Sluijs, A., Röhl, U., Schouten, S., Brumsack, H. J., Sangiorgi, F., Sinninghe Damsté, J. S., and Brinkhuis, H.: Article late Paleocene - Early Eocene paleoenvironments with special emphasis on the Paleocene-Eocene thermal maximum (Lomonosov Ridge, Integrated Ocean Drilling Program Expedition 302), *Paleoceanography*, 23, 1–17, doi:10.1029/2007PA001495, 2008.
- 1080 Sluijs, A., Zeebe, R. E., Bijl, P. K., and Bohaty, S. M.: A middle Eocene carbon cycle conundrum, *Nature Geoscience*, 6, 429–434, doi:10.1038/ngeo1807, <http://dx.doi.org/10.1038/ngeo1807>, 2013.



- Smith, G. A., Manchester, S. R., Ashwill, M., McIntosh, W. C., and Conrey, R. M.: Late Eocene-early Oligocene tectonism, volcanism, and floristic change near Gray Butte, central Oregon, *Bulletin of the Geological Society of America*, 110, 759–778, doi:10.1130/0016-7606(1998)110<0759:LLEOTV>2.3.CO;2, 1998.
- Smith, R. D. and McWilliams, J. C.: Anisotropic horizontal viscosity for ocean models, *Ocean Modelling*, 5, 129–156, doi:10.1016/S1463-5003(02)00016-1, 2003.
- 1085 Smith, R. D., Jones, P., Briegleb, B., Bryan, F., Danabasoglu, G., Dennis, J., Dukowicz, J., Eden, C., Fox-Kemper, B., Gent, P., Hecht, M., Jayne, S., Jochum, M., Large, W., Lindsay, K., Maltrud, M., Norton, N., Peacock, S., Vertenstein, M., and Yeager, S.: The Parallel Ocean Program (POP) reference manual: Ocean component of the Community Climate System Model (CCSM), Los Alamos National Laboratory Tech. Rep. LAUR-10-01853, 141, 1–141, www.cesm.ucar.edu/models/cesm1.0/pop2/doc/sci/POPRefManual.pdf, 2010.
- 1090 Song, X. and Zhang, G. J.: Convection parameterization, tropical pacific double ITCZ, and upper-ocean biases in the NCAR CCSM3. Part II: Coupled feedback and the role of ocean heat transport, *Journal of Climate*, 23, 800–812, doi:10.1175/2009JCLI3109.1, 2009.
- 1095 Steele, M., Morley, R., and Ermold, W.: PHC: A global ocean hydrography with a high-quality Arctic Ocean, *Journal of Climate*, 14, 2079–2087, doi:10.1175/1520-0442(2001)014<2079:PAGOHW>2.0.CO;2, 2001.
- Stickley, C. E., Brinkhuis, H., Schellenberg, S. a., Sluijs, A., Röhl, U., Fuller, M., Grauert, M., Huber, M., Warnaar, J., and Williams, G. L.: Timing and nature of the deepening of the Tasmanian Gateway, *Paleoceanography*, 19, 1–18, doi:10.1029/2004PA001022, 2004.
- 1100 Stickley, C. E., St John, K., Koç, N., Jordan, R. W., Passchier, S., Pearce, R. B., and Kearns, L. E.: Evidence for middle Eocene Arctic sea ice from diatoms and ice-rafted debris, *Nature*, 460, 376–379, doi:10.1038/nature08163, 2009.
- Thiele, G. and Sarmiento, J.: Tracer Dating and Ocean Ventilation, *Journal of Geophysical Research*, 95, 9377–9391, doi:10.1029/JC095iC06p09377, http://www.agu.org/pubs/crossref/1990/JC095iC06p09377.shtml, 1990.
- 1105 Traiser, C., Klotz, S., Uhl, D., and Mosbrugger, V.: Environmental signals from leaves—a physiognomic analysis of European vegetation., *The New phytologist*, 166, 465–484, doi:10.1111/j.1469-8137.2005.01316.x, 2005.
- Trenberth, K. E. and Caron, J. M.: Estimates of Meridional Atmosphere and Ocean Heat Transports, *Journal of Climate*, 14, 3433–3443, doi:10.1175/1520-0442(2001)014<3433:EOMAAO>2.0.CO;2, 2001.
- 1110 Tripathi, A. K. and Zachos, J.: Late Eocene tropical sea surface temperatures : A perspective from Panama, 17, 2002.
- Tripathi, A. K., Delaney, M. L., Zachos, J. C., Anderson, L. D., Kelly, D. C., and Elderfield, H.: Tropical sea-surface temperature reconstruction for the early Paleogene using Mg/Ca ratios of planktonic foraminifera, *Paleoceanography*, 18, doi:10.1029/2003PA000937, 2003.
- 1115 Uhl, D., Klotz, S., Traiser, C., Thiel, C., Utescher, T., Kowalski, E., and Dilcher, D. L.: Cenozoic paleotemperatures and leaf physiognomy - A European perspective, *Palaeogeography, Palaeoclimatology, Palaeoecology*, 248, 24–31, doi:10.1016/j.palaeo.2006.11.005, 2007.
- van Hinsbergen, D. J. J., de Groot, L. V., van Schaik, S. J., Spakman, W., Bijl, P. K., Sluijs, A., Langereis, C. G., and Brinkhuis, H.: A Paleolatitude Calculator for Paleoclimate Studies, *PLoS One*, 10, doi:10.1371/journal.pone.0126946, 2015.
- 1120



- Viebahn, J. P., von der Heydt, A. S., Le Bars, D., and Dijkstra, H. A.: Effects of Drake Passage on a strongly eddying global ocean, *Paleoceanography*, 31, 564–581, doi:10.1002/2015PA002888, 2016.
- Wade, B. S., Houben, A. J., Quaijtaal, W., Schouten, S., Rosenthal, Y., Miller, K. G., Katz, M. E., Wright, J. D., and Brinkhuis, H.: Multiproxy record of abrupt sea-surface cooling across the Eocene-Oligocene transition in the Gulf of Mexico, *Geology*, 40, 159–162, doi:10.1130/G32577.1, 2012.
- 1125 Wing, S. and Greenwood, D.: Fossils and fossil climate: The case for equable continental interiors in the Eocene, *Philosophical Transactions of the Royal Society of London B Biological Sciences*, 341, 243–252, doi:10.1098/rstb.1993.0109, 1993.
- Wolfe, J. A., Forest, C. E., and Molnar, P.: Paleobotanical evidence of Eocene and Oligocene paleoaltitudes in midlatitude western North America, *Bulletin of the Geological Society of America*, 110, 664–678, doi:10.1130/0016-7606(1998)110<0664:PEOEAO>2.3.CO;2, 1998.
- 1130 Yang, J., Spicer, R. A., Spicer, T. E., and Li, C. S.: 'CLAMP Online': A new web-based palaeoclimate tool and its application to the terrestrial Paleogene and Neogene of North America, *Palaeobiodiversity and Palaeoenvironments*, 91, 163–183, doi:10.1007/s12549-011-0056-2, 2011.
- 1135 Ye, D.-Z. and Wu, G.-X.: The role of the heat source of the Tibetan Plateau in the general circulation, *Meteorology and Atmospheric Physics*, 67, 181–198, doi:10.1007/BF01277509, <https://link.springer.com/article/10.1007/BF01277509>, 1998.
- Zachos, J. C., Stott, D., and Lohmann, K. C.: Evolution of early Cenozoic marine temperatures at Equator, *Paleoceanography*, 9, 353–387, doi:10.1029/93PA03266, 1994.
- 1140 Zachos, J. C., Pagani, M., Sloan, L., Thomas, E., and Billups, K.: Trends, rhythms, and aberrations in global climate 65 Ma to present., *Science*, 292, 686–693, doi:10.1126/science.1059412, 2001.
- Zachos, J. C., Dickens, G. R., and Zeebe, R. E.: An early Cenozoic perspective on greenhouse warming and carbon-cycle dynamics., *Nature*, 451, 279–283, doi:10.1038/nature06588, 2008.
- Zhu, J., Poulsen, C. J., and Tierney, J. E.: Simulation of Eocene extreme warmth and high climate sensitivity through cloud feedbacks, pp. 1–11, 2019.
- 1145